Goethe-Universität Frankfurt am Main
Fachbereich 13 Physik
Institut für theoretische Physik

Master Thesis

Hybrid static potentials at small lattice spacings and possible glueball decay

Carolin Riehl

26. September 2019

Supervisor: Prof. Dr. Marc Wagner
Second supervisor: Prof. Dr. Owe Philipsen

Erklärung nach § 30 (12) Ordnung für den Bachelor- und dem Masterstudiengang

Hiermit erkläre ich, dass ich die Arbeit selbstständig und ohne Benutzung anderer als der angegebenen Quellen und Hilfsmittel verfasst habe. Alle Stellen der Arbeit, die wörtlich oder sinngemäß aus Veröffentlichungen oder aus anderen fremden Texten entnommen wurden, sind von mir als solche kenntlich gemacht worden. Ferner erkläre ich, dass die Arbeit nicht - auch nicht auszugsweise - für eine andere Prüfung verwendet wurde.

Frankfurt am Main, den 26. September 2019

(Carolin Riehl)

Abstract

The aim of this work is the investigation of hybrid static potentials at short quark-antiquark separations and a possible decay into the ordinary static potential and a glueball. We define a creation operator for the decay product state with quantum numbers identical to hybrid static potentials. On this basis, we can exclude a decay of hybrid potentials Σ_u^- and Σ_g^- into the lightest glueball 0^{++}. Furthermore, separation distances are determined below which lattice hybrid potential data will be contaminated by an energetically allowed glueball decay.
We compute the ordinary static potential Σ_g^+ and the lowest hybrid potential Π_u in $SU(2)$ pure gauge theory at $\beta = 2.50$, 2.70, 2.85 and 3.00 and the mass of 0^{++}-glueball with an optimized operator at $\beta = 2.50$, 2.85 and 3.00. The study of static potentials and glueball at small lattice spacings serves as a preparation for future lattice computations of hybrid static potentials at short distances.

Contents

1 Introduction **1**

1.1 Outline . . . 2

I Theory **3**

2 Lattice gauge theory **4**

2.1 Path integral formalism . . . 4

2.2 Statistical analysis . . . 6

2.3 Static potentials . . . 7

2.3.1 Symmetry group . . . 7

2.3.2 Operators . . . 9

2.4 Glueballs . . . 11

2.4.1 Symmetry group . . . 12

2.4.2 Operator . . . 12

2.4.3 Smearing . . . 13

2.5 Lattice scale setting . . . 14

3 Decay of excited static potentials into glueballs **19**

3.1 Direct product representations . . . 19

3.2 Operator of decay states . . . 20

3.2.1 Possible quantum numbers . . . 22

3.3 Momentum projection . . . 23

3.4 Decay threshold . . . 24

II Lattice results **28**

4 Static potentials at small lattice spacings **29**

4.1 Ordinary static potential Σ_g^+ . . . 29

4.2 Hybrid static potential Π_u . . . 34

5 Glueballs at small lattice spacings **38**

5.1 Optimization of blocking and smearing steps . . . 38

5.2 Glueball mass . . . 41

6 Conclusion **43**

6.1 Summary . . . 43

6.2 Outlook . . . 43

Appendices **44**

A Cylindrical wave expansion of plane waves **45**

A.1 Solution of free Schrödinger equation in cylindrical coordinates 45

A.2 Expansion of plane waves 46

A.3 Fourier transform of $J_l(kr)e^{il\varphi}$ 47

1 Introduction

The strong interaction between quarks and gluons, which is one of the fundamental forces, is described by Quantum Chromodynamics. Besides conventional hadrons, Quantum Chromodynamics allows for the existence of glueballs, which are predominantly gluonic bound states, and exotic mesons. Exotic mesons are composites of quarks and gluons which have a non-trivial structure different from an ordinary quark-antiquark pair. Due to their exotic structure, quantum numbers can be different from those predicted by the constituent quark model.
In experiments, heavy quarkonium states with exotic properties have been observed which are called XYZ mesons (cf. e.g. [1]). There exist different interpretations of such exotic states (cf. e.g. [2–5]). One possibility is the tetraquark, which forms a four-quark system. Another system able to create exotic quantum numbers is the hybrid meson. It consists of a quark and an antiquark with an excited gluon field, which contributes to the system's quantum numbers.

Exotic mesons and glueballs are a current topic of investigation, both in theory and in experiments. Facilities like PANDA at FAIR plan to search for exotic mesons and glueballs as they confirm the validity of Quantum Chromodynamics as the theory of the strong interaction.
In theory, heavy hybrid mesons are studied in Lattice Quantum Chromodynamics. The computation of masses works within the Born-Oppenheimer approximation, also applied for diatomic molecules [6]. Assuming heavy quark masses, i.e. the static limit, the gluonic energies can be obtained. Lattice results of static potentials in the limit of infintely heavy quarks are computed and parametrized [7]. The static potentials serve as an input in the Schrödinger equation solved for the mass of hybrid mesons.
To gain a reliable parametrization, in particular at small separation distances, lattice data is required. Computations on very fine lattices have to be performed to obtain hybrid potential lattice results at short distances. They are, for example, also required to fix nonperturbative parameters in the description of hybrid potentials in nonrelativistic effective field theories [8]. So far, analyses of hybrids rely on potential data starting at separations of $r \approx 0.1\,\mathrm{fm}$ (cf. e.g. [7, 9, 10]).

The aim of this work is to investigate hybrid static potentials at very small separation distances. We discuss possible decays of hybrid static potentials through the emission of glueballs at small separations where the static energy difference to the ordinary potential is sufficiently high. The lowest hybrid static potential and glueball are both computed on very fine lattices to get insight in the short distance behavior of static potentials and the occuring difficulties and necessary steps in the computations at small lattice spacings.

1.1 Outline

This thesis is organized as follows.
In the first part, Chapter 2, we introduce basic concepts of Lattice Quantum Chromodynamics. Definitions and symmetry aspects of static potentials and glueballs and their creation operators are presented. Furthermore, methods of lattice scale setting are reviewed and compared to the weak-coupling limit solution of the renormalization group equation.
In Chapter 3, the decay of excited static potentials is investigated. Operators for a decay product trial state of ordinary static potential and glueball are presented. On this basis, we identify hybrid static potentials that are excluded from a decay into the lightest glueball. Furthermore, we determine quark-antiquark distances at which hybrid static potentials reach the minimal energy for a possible decay.
Finally, lattice results are presented. In Chapter 4, static potentials are computed at differently fine lattices and arising difficulties due to the small lattice spacings are discussed. Moreover, we compare results for different scale settings. In Chapter 5, glueball mass computations at small lattice spacings are investigated. The optimal smearing procedure is worked out and the glueball mass is computed. In the end, results are summarized.

Part I

Theory

2 Lattice gauge theory

Quantum Chromodynamics (QCD) is the theory of the strong force. It describes the interaction between quarks and gluons. Due to the energy dependence of its coupling, the large energy regime can be studied with perturbation theory as the coupling is small. On the contrary, the low energy regime is not accessible perturbatively due to the large coupling. With Lattice QCD, quantities in the low energy regime like hadron masses can be computed numerically. By discretizing spacetime and use of numerical algorithms, Lattice QCD enables the computation of path integrals which constitute one framework to formulate the theory of QCD.

Commonly, Lattice QCD is formulated on a four-dimensional hypercubic lattice with temporal and spatial extensions, $T \times L^3$. Lattice sites are separated by a distance a, which is not known at the beginning. It has to be determined through a scale setting procedure in order to obtain physical results. In this thesis, four-dimensional $SU(2)$ Yang-Mills theory is applied as it builds a good starting point, since it is much simpler to simulate than full gauge theory including fermions. However, pure gauge theory is already able to reveal relevant phenomena for gluonic observables which are of interest in this thesis.

In the following, the basic concepts of lattice gauge theory are introduced based on [11, 12].

2.1 Path integral formalism

The starting point for the framework of path integrals is the partition function

$$Z = \int DA_\mu e^{-S[A]}, \tag{2.1}$$

where $S[A] = \frac{1}{4}\int \mathrm{d}^4x\, F^a_{\mu\nu}F^a_{\mu\nu}$ is the Euclidean gauge action with the field strength tensor $F_{\mu\nu}$. The integration measure contains all possible fields at all points in the spacetime volume. Accordingly, the integration is performed over all possible gauge field configurations weighted with the gauge action, which introduces the quantization of the field theory in the path integral formalism.
To use this framework on the lattice, a discretization of fields has to be performed. Instead of using the continuum gauge field A_μ, the path integral is expressed in terms of link variables $U_\mu \in SU(N)$, which build the links between lattice sites. The lattice link is related to the continuum gauge field via

$$U_\mu(n) = \exp(-iaA_\mu(n)), \tag{2.2}$$

where a denotes the spacing between two neighboring lattice sites. This link variable connects the lattice point n with the next lattice site in μ direction.
There exist various discretizations of the continuum action which are suitable for different appli-

cations. The simplest discretization is the *Wilson plaquette action*:

$$S = \beta \sum_{x \in \Gamma} \sum_{\mu < \nu} \frac{1}{2N} \operatorname{Re} \operatorname{Tr} \left[1 - U_{\mu\nu}(x) \right]. \tag{2.3}$$

It is expressed through a sum over all lattice points $x \in \Gamma$ and all orientiations of the plaquette $U_{\mu\nu}(x)$, which is defined as the smallest closed loop of lattice link variables

$$U_{\mu\nu}(x) = U_{\mu}(x) U_{\nu}(x + \hat{\mu}) U_{-\mu}(x + \hat{\mu} + \hat{\nu}) U_{-\nu}(x + \hat{\nu}). \tag{2.4}$$

The factor β in the action denotes the *lattice coupling*, which is related to the bare coupling via $\beta = \frac{2N}{g^2}$. This parameter sets the scale in a simulation of *SU(N)* Yang-Mills theory on the lattice. In the naive continuum limit, i.e. $a \to 0$, the Wilson plaquette action yields the correct continuum action with discretization error of $\mathcal{O}\left(a^2\right)$. As the continuous action, the discretization (2.3) is gauge invariant.

Observables In the path integral formalism for pure gauge theory, a correlation function of an operator $\mathcal{O}$ creating a state with the quantum numbers of interest from the vacuum $|\Omega\rangle$ can be written as follows

$$C(t) = \langle \Omega | \mathcal{O}^{\dagger}(t) \mathcal{O}(0) | \Omega \rangle = \int DA_{\mu} \; \mathcal{O}^{\dagger}(t) \mathcal{O}(0) \; e^{-S[A_{\mu}]}. \tag{2.5}$$

With the Euclidian time evolution operator and a set of energy eigenvalues, the correlation function can be expressed as a sum over the energy eigenstates of exponentials of energy differences

$$C(t) = \langle \Omega | \mathcal{O}^{\dagger}(t) \mathcal{O}(0) | \Omega \rangle = \sum_{n} | \langle n | \mathcal{O}(0) | \Omega \rangle |^2 \; e^{-(E_n - E_{\Omega})t} \tag{2.6}$$

$$\overset{t \to \infty}{=} \quad | \langle 0 | \mathcal{O}(0) | \Omega \rangle |^2 \; e^{-(E_0 - E_{\Omega})t}. \tag{2.7}$$

In the large time limit, the higher excitations are suppressed so that the groundstate energy difference to the vacuum dominates the correlation function. The prefactor denotes the overlap of the state created by the operator with the groundstate. On this basis, non-perturbative quantities like masses can be extracted from the exponential decay of correlation functions measured on the lattice. In practice, the effective mass,

$$a m_{\text{eff}}(t) = \ln\left(\frac{C(t)}{C(t + a)} \right), \tag{2.8}$$

is examined as it approaches a plateau in the large time limit which constitutes the mass in lattice units one is interested in.

Correlators are expressed in terms of gauge links on the lattice. Since the signal-to-noise ratio decreases rapidly with t, it is important that the operator overlap to excited states is minimized. In common tasks like the computation of static potentials, the overlap to the groundstate can be increased by defining non-local operators. This is done by adding weigthed averages over neigboring links to single links contributing to the operator. This procedure is known as *link smearing*. A commonly applied technique is *APE-smearing* [13]. The link variable $U_{\mu}^{(N_{\text{APE}}-1)}(x)$

is replaced in the N_{APE}-th smearing step by

$$U_\mu^{N_{\mathrm{APE}}}(x) = P_{SU(N)}\left[(1-\alpha)\,U_\mu^{(N_{\mathrm{APE}}-1)}(x) + \frac{\alpha}{6}\sum_{\mu\neq\pm\nu}\tilde{V}_{\mu\nu}^{(N_{\mathrm{APE}}-1)}(x)\right], \tag{2.9}$$

where $\tilde{V}_{\mu\nu}^{(N_{\mathrm{APE}}-1)}(x) = U_\nu^{(N_{\mathrm{APE}}-1)}(x)U_\mu^{(N_{\mathrm{APE}}-1)}(x+\hat{\nu})U_{-\nu}^{(N_{\mathrm{APE}}-1)}(x+\hat{\nu}+\hat{\mu})$ is the staple surrounding the link. Common choices for the parameters are $N_{\mathrm{APE}} = 20$ and $\alpha = 0.5$ which proved to be suitable for the computation of static potentials [7]. In this thesis, all spatial link variables used in the computation of static potentials are APE-smeared. Besides single-link smearing like APE-smearing, we find that double-link smearing is useful in the case of glueball mass computation, which will be discussed later.

2.2 Statistical analysis

Lattice QCD evaluates path integrals for correlation functions on a large set of gauge field configurations which are distributed according to the gauge action serving as a weight factor. To provide such a distribution for a statistical analysis of observables, Monte Carlo algorithms are applied. A Monte Carlo heatbath algorithm is used in this thesis for the generation of gauge field configurations in $SU(2)$.
Before configurations can be used for measurements, the updating algorithm has to pass thermalization phase until the generated set of configurations reaches the desired equilibrium distribution. Furthermore, not only the first updates before thermalization should be discarded, but intermediate configurations as well, since subsequently generated configurations are correlated. Algorithms are based on Markov chains, where the updated gauge field depends on the previous state.
The evaluation of a simple observable, the plaquette $U_{\mu\nu}(x)$, on each configuration can serve as a check for thermalization and autocorrelation time being distinct for each lattice setup.

An observable of interest θ is estimated from a set of measurements, which is obtained on a large number of configurations. The statistical error of the observable is obtained via the *jackknife method*.
From the full sample of measurements, one starts with building M bins containing K data values. Through binning correllated data appropriately, autocorrelations can be removed. Next, one constructs inverse bins,

$$\tilde{X}_i = \frac{1}{M-1}\left[\sum_{m=1}^{M} X_m - X_i\right], \tag{2.10}$$

by deleting one bin average. With the observables estimated from the inverse bins, θ_i, the error estimate of the observable is given by

$$\sigma_\theta = \sqrt{\frac{M-1}{M}\sum_{i=1}^{M}\left(\theta_i - \hat{\theta}\right)^2}, \tag{2.11}$$

where $\hat{\theta}$ is the estimate obtained from the full sample.
In this thesis, all of the given errors denote statistical errors obtained from a jackknife analysis

starting at the level of correlation functions.

2.3 Static potentials

A quark and an antiquark separated by a distance r are surrounded by a gluon field. The gluonic energy can be studied in the static limit, where one assumes the quarks to be infinitely heavy. In the case of heavy quarks like charm or bottom, this constitutes a reasonable assumption. Since hybrid mesons show the same symmetries as diatomic molecules, their description is partly similar. The energy of the gluonic degrees of freedom in the static limit is given by the ordinary static potential labelled with Σ_g^+.

Furthermore, the gluon field between a static quark and an antiquark can be excited. This additional excitation contributes to the quantum numbers of the system. A static potential with an excited gluon field is called *hybrid static potential*.
The static potentials are functions of relative distance between the quark and antiquark. The ordinary static potential is parametrized by the known Cornell potential

$$V_{\Sigma_g^+}(r) = V_0 - \frac{\alpha}{r} + \sigma r, \tag{2.12}$$

where V_0 is an unphysical constant and the second term implies the expected attractive behavior from perturbation theory. The linear rise of the potential is proportional to σ, which denotes the string tension. This shape is explained by color confinement. Pulling the quarks apart leads to a linear rise of energy between them, and thus no free quarks will be observable.
Parametrizations for the two lowest hybrid static potentials, Π_u and Σ_u^-, have been derived in [7]. The static energy Π_u is well described by

$$V_{\Pi_u}(r) = \frac{A_1}{r} + A_2 + A_3 r^2. \tag{2.13}$$

The form of this parametrization is based on pNRQCD predictions for static potentials which are valid at small separations [8]. The constant A_2 denotes an unphysical shift. In contrast to the groundstate, the hybrid static potential parametrization has a repulsive $1/r$ dependence at short distances. This is the expected leading order term of the octet potential $V_o(r)$ obtained in perturbation theory in the short-distance limit. The next order correction is given by a quadratic term in r, which is necessary to form bound states.

In the upcoming sections, a short introduction is given to the relevant symmetry group and group theoretical basics for the description of trial states on the lattice [14, 15]. Afterwards, we outline how creation operators for the ordinary static potential as well as hybrid static potentials are defined, according to [7].

2.3.1 Symmetry group

Static potentials are classified according to the system's behavior under symmetry transformations belonging to the infinite dihedral point group $D_{\infty h}$.
The quantum numbers specify the properties of the state under those symmetry transformations: $\Lambda = \Sigma, \Pi, \Delta, ...$ denotes non-negative integer values of angular momentum with respect to

$D_{\infty h}$	D_{4h}
$A_{1g} = \Sigma_g^+$	A_{1g}
$A_{2g} = \Sigma_g^-$	A_{2g}
$A_{1u} = \Sigma_u^+$	A_{1u}
$A_{2u} = \Sigma_u^-$	A_{2u}
$E_{1g} = \Pi_g$	E_g
$E_{1u} = \Pi_u$	E_u
$E_{2g} = \Delta_g$	$B_{1g} + B_{2g}$
$E_{2u} = \Delta_u$	$B_{1u} + B_{2u}$
$E_{3g} = \Phi_g$	E_g
$E_{3u} = \Phi_u$	E_u
$\vdots$	$\vdots$

Table 2.1: Correlation table between irreducible representations of the infinite group $D_{\infty h}$ and the finite subgroup D_{4h}.

rotation around the quark separation axis. $\eta = g, u$ describes the even (g) or odd (u) behavior under combined parity transformation and charge conjugation, $\mathcal{P} \circ \mathcal{C}$. Finally, $\epsilon = +, -$ is the eigenvalue of reflection along an axis perpendicular to the quark separation axis, $\mathcal{P}_x$. However, hybrid static potentials with $\Lambda \geq 1$ are degenerate with respect to ϵ.
The combination Λ_η^ϵ designates states in an irreducible representation of the infinite point group $D_{\infty h}$.
The dihedral group has four one-dimensional representations, conventionally labelled with A_{1g}, A_{2g}, A_{1u}, A_{2u} which correspond to quantum numbers Σ_g^+, Σ_g^-, Σ_u^+, Σ_u^-, respectively. The two-dimensional representations are denoted by E. As an example, the groundstate static potential transforms according to the trivial representation A_{1g}, hence, it is labelled with quantum numbers $\Lambda_\eta^\epsilon = \Sigma_g^+$.

When spacetime is discretized, the continuous symmetry group $D_{\infty h}$ is broken into its finite subgroup D_{4h}. It has a finite number of irreducible representations due to the restriction to the rotation angle $\varphi = 2\pi n/4, n = 0, 1, 2, 3$ on a spacetime lattice considering only nearest neighbors. Out of ten irreducible representations, there are eight one-dimensional representations labelled by A and B and two two-dimensional ones denoted by E.
Because irreducible representations of a group are reducible in a subgroup, states constructed in the discrete representation could belong to more than one representation of the continuous group. The correlation between irreducible representations of the continuous group and the subduced representations of its finite subgroup is presented in Table 2.1. Continuing the list to higher angular momentum, the irreducible representations of the finite group appear multiple times. However, in general, it can be expected that a potential in a representation of the finite group computed on the lattice belongs to the lowest angular momentum in the continuum as higher energies are suppressed in the correlator at large times. Thus, in the following, we denote states, which are in a representation of D_{4h}, with quantum numbers Λ_η^ϵ, which label states in the lowest induced representation.

In the definition of creation operators for states transforming in a specific representation, one makes use of the *Wigner-Eckart theorem*.

This theorem concerns matrix elements of irreducible tensor operators.
A set of d_q operators transforming under a symmetry operation $P(T)$ as a basis of an irreducible representation Γ^q of the group G, i.e. fulfilling

$$P(T)\mathcal{Q}_j^q P^\dagger(T) = \sum_{k=1}^{d_q} \Gamma_{kj}^q(T)\mathcal{Q}_k^q, \tag{2.14}$$

are called *irreducible tensor operators*. d_q denotes the dimension of the representation Γ^q.
An irreducible tensor operator can also be defined as the multiplication of a basis function ψ_j^q for the irreducible representation Γ^q

$$\mathcal{Q}_j^q f = \psi_j^q f. \tag{2.15}$$

In case of the infinite dihedral group $D_{\infty h}$, the basis function for the representation Λ is $\exp(i\Lambda\varphi)$.
As one useful application, the Wigner-Eckart theorem provides a selection rule for quantum numbers [16]. It states that the matrix element of the irreducible tensor operator with respect to basis vectors of different representations $\langle m'|\mathcal{Q}^q|m\rangle$ is only non-vanishing if $m' = m + q$. This means that the irreducible tensor operator, which acts on the state $|m\rangle$, adds the quantum number q.
In summary, an irreducible tensor operator of an irreducible representation will create a state from the vacuum which transforms exactly according to this representation.

2.3.2 Operators

Ordinary static potential

The simplest operator creating a state with quantum numbers Σ_g^+ is

$$\mathcal{O}_{\Sigma_g^+}(\vec{x}) = \bar{q}(\vec{x} - r/2\hat{e}_z)U(\vec{x} - r/2\hat{e}_z, \vec{x} + r/2\hat{e}_z)q(\vec{x} + r/2\hat{e}_z), \tag{2.16}$$

where q and $\bar{q}$ create a quark and an antiquark in a distance $r/2$ along the z-direction from the position $\vec{x}$, respectively. They are connected by a straight path of parallel transporters along the separation axis.
The generated state transforms according to the trivial representation of the dihedral group, Σ_g^+: It is obvious that this state is invariant under rotations around the separation axis by an angle φ that implies $\Lambda = \Sigma$. Parity transformation and charge conjugation yield $\eta = g$, designating an even behavior. Reflection along an axis perpendicular to the separation axis has obviously no effect, consequently, $\epsilon = +$.

Computing the temporal correlation function on the lattice amounts in the computation of ordinary Wilson loops

$$W(r,t) = \mathrm{Tr}\left[U_z(-r/2, r/2; 0)U_t(r/2; 0, t)U_z^\dagger(-r/2, r/2; t)U_t^\dagger(-r/2; 0, t)\right]. \tag{2.17}$$

They are closed loops of parallel transporters in spatial direction $U_z(-r/2, r/2; 0)$ connecting lattice points $(-r/2; 0)$ and $(r/2; 0)$ along the quark separation axis and in temporal direction, $U_t(r/2; 0, t)$ connecting lattice sites $(r/2; 0)$ and $(r/2; t)$.

Hybrid static potentials

If the gluon field between the quark and antiquark is excited, it influences the symmetry of the state. This results in different quantum numbers. The contribution of gluonic excitations can be included in a creation operator by introducing an additional structure along the separation axis. The operator reads

$$\mathcal{O}_S(\vec{x}) = \bar{q}(\vec{x} - r/2\hat{e}_z)U(\vec{x} - r/2\hat{e}_z, \vec{r}_1)S(\vec{r}_1, \vec{r}_2)U(\vec{r}_2, \hat{x} + r/2\hat{e}_z)q(\vec{x} + r/2\hat{e}_z), \tag{2.18}$$

where $S(\vec{r}_1, \vec{r}_2)$ is a non-trivial path inserted between r_1 and r_2 on the separation axis. This insertion represents the gluonic excitation. The exact form of insertion S should be chosen such that it exhibits the correct symmetry under the action of inversion of the axis perpendicular to the separation axis and the combination of parity and charge conjugation. Its shape should also be able to reproduce the desired angular momentum and have high overlap with the state of interest.
To ensure that the state created from the vacuum has well defined quantum numbers, one makes use of the Wigner-Eckart theorem.
An irreducible tensor operator, which creates a hybrid trial state with well defined angular momentum Λ from the vacuum, is given by

$$\mathcal{O}_\Lambda = \int_0^{2\pi} \mathrm{d}\varphi \exp(i\Lambda\varphi) R(\varphi)\mathcal{O}_S. \tag{2.19}$$

This operator is indeed an irreducible tensor operator which can be confirmed through the following rotation operation:

$$\begin{aligned} R(\alpha)\mathcal{O}_\Lambda R^\dagger(\alpha) &= \int_0^{2\pi} \mathrm{d}\varphi \exp(i\Lambda\varphi) R(\varphi + \alpha)\mathcal{O}_S & (2.20)\\ &= \int_0^{2\pi} \mathrm{d}\varphi' \exp\big(i\Lambda\varphi' - \alpha\big) R(\varphi')\mathcal{O}_S & (2.21)\\ &= \exp(-i\Lambda\alpha)\mathcal{O}_\Lambda. & (2.22) \end{aligned}$$

Here, $\exp(-i\Lambda\alpha)$ is the element of irreducible representation Λ. According to the Wigner-Eckart-theorem, this operator adds the quantum number Λ to the vacuum.
So far, the operator has no well defined behavior under the discrete symmetry operations of $\mathcal{P}_x$ and $\mathcal{P}\circ\mathcal{C}$. This can be fixed by projecting the trial state created by operator $\mathcal{O}_\Lambda$ onto eigenstates of these symmetry operations with projectors

$$\mathbb{P}_{\mathcal{P}\circ\mathcal{C}} = \frac{1}{2}\left(1 + \eta\left(\mathcal{P}\circ\mathcal{C}\right)\right) \qquad \text{and} \qquad \mathbb{P}_{\mathcal{P}_x} = \frac{1}{2}\left(1 + \epsilon\mathcal{P}_x\right). \tag{2.23}$$

The operator

$$\mathcal{O}_{\Lambda^\epsilon_\eta} = \mathbb{P}_{\mathcal{P}\circ\mathcal{C}}\ \mathbb{P}_{\mathcal{P}_x} \int_0^{2\pi} \mathrm{d}\varphi \exp(i\Lambda\varphi) R(\varphi)\mathcal{O}_S, \tag{2.24}$$

with an appropriate insertion S creates a trial state with quantum numbers Λ^ϵ_η from the vacuum. On the lattice, the rotation angle is restricted to $k\pi/2, k = 0, 1, 2, 3$. The operator becomes a discrete sum of properly weighted rotations and reflections of the original operator. The lattice

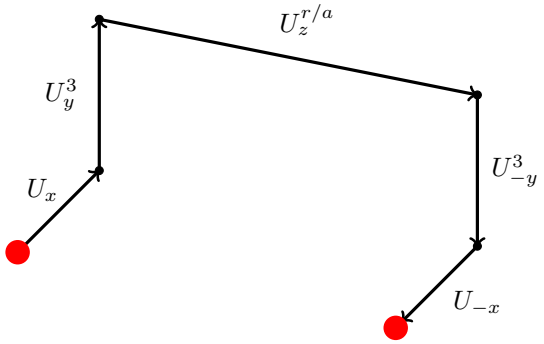

Figure 2.1: Illustration of insertion $US_{\mathrm{III},1}U = U_x U_y^3 U_z^{r/a} U_{-y}^3 U_{-x}$.

operator is given by

$$\mathcal{O}_{\Lambda_\eta^\epsilon} = \frac{1}{4}\Big(1 + \eta\,(\mathcal{P}\circ\mathcal{C}) + \epsilon\mathcal{P}_x + \eta\epsilon\,(\mathcal{P}\circ\mathcal{C})\,\mathcal{P}_x\Big)\sum_{k=0}^{3}\exp\left(\frac{i\pi\Lambda k}{2}\right)R\left(\frac{\pi k}{2}\right)\mathcal{O}_S. \tag{2.25}$$

In contrast to the ordinary static potential, hybrid Wilson loops computed on the lattice are closed loops with non-trivial shapes in the spatial direction instead of straight paths of lattice links

$$W_{\Lambda_\eta^\epsilon} = \mathrm{Tr}\left[a_{\Lambda_\eta^\epsilon}(-r/2,+r/2;0)U_t(r/2;0,t)a^\dagger_{\Lambda_\eta^\epsilon}(-r/2,r/2;t)U_t^\dagger(-r/2;0,t)\right], \tag{2.26}$$

with

$$\begin{aligned} a_{\Lambda_\eta^\epsilon}(-r/2,+r/2;0) = \frac{1}{4}\Big(1 + \eta\,(\mathcal{P}\circ\mathcal{C}) + \epsilon\mathcal{P}_x + \eta\epsilon\,(\mathcal{P}\circ\mathcal{C})\,\mathcal{P}_x\Big) \\ \sum_{k=0}^{3}\exp\left(\frac{i\pi\Lambda k}{2}\right)R\left(\frac{\pi k}{2}\right)\Big(U(-r/2,r_1)S(r_1,r_2)U(r_2,r/2)\Big). \end{aligned} \tag{2.27}$$

The optimal form and length of insertions for hybrid static potentials, which maximize their groundstate overlap, were found in [7]. To generate a state with quantum numbers Π_u, which constitutes the lowest hybrid static potential, we choose $US_{\mathrm{III},1}U = U_x U_y^3 U_z^{r/a} U_{-y}^3 U_{-x}$, illustrated in Figure 2.1, in our computation at small lattice spacings.
The extension along the axis of separation, denoted by z, corresponds to the relative separation r/a of the quark and antiquark. Thus, $U_z^{r/a}$ represents the product of r/a successive gauge links U_z in z-direction.

2.4 Glueballs

QCD allows for the formation of bound states from gluonic fields. The so called *glueballs* are searched in experiments to investigate QCD as the theory of the strong interaction. Lattice QCD provides the possibility to compute the mass spectrum of glueballs.
In the following, a brief introduction to the symmetry group and creation operators of glueballs is given, before methods are presented to improve the signal of correlators measured on the lattice.

Continuum spin J	O_h
0	A_1
1	T_1
2	$E + T_2$
3	$A_2 + T_1 + T_2$
4	$A_1 + E + T_1 + T_2$
$\vdots$	$\vdots$

Table 2.2: Correlation table between spin representations of the infinite rotation group J and the representations in the finite subgroup O_h.

2.4.1 Symmetry group

In continuum, the symmetry group of glueballs is the three-dimensional rotation group $SO(3)$ combined with parity and charge conjugation. The transformation properties define the quantum numbers J^{PC}, labelling the irreducible representations of the symmetry group.
The discretized spacetime on the lattice breaks the continuous rotational symmetry. The symmetry group of zero-momentum glueballs on the lattice is the full cubic group O_h containing discrete rotations and reflections.
The discrete group has four one-dimensional irreducible representations named $A_1^{\pm}, A_2^{\pm}$, two two-dimensional, $E^{\pm}$ and four three-dimensional irreducible representations $T_1^{\pm}, T_2^{\pm}$.
Since the full cubic group O_h is a subgroup of the continuous rotation group, representations J of the continuum can be decomposed into irreducible representations of the finite group. States transforming according to representations of the subgroup contribute to more than one spin representation J in the continuum if it appears in the subduced representation of J. The subduced representations of $SO(3)$ in O_h are presented in Table 2.2. Due to the expected suppression of higher angular momentum in the correlator at large times, states in a representation of the finite subgroup will be identified with the lowest corresponding spin state and will be labelled accordingly.

2.4.2 Operator

The temporal correlator $C(t)$ includes the operator $\mathcal{O}_{J^{PC}}$ creating a glueball transforming according to the representation J combined with the discrete symmetries of parity and charge conjugation.
In this thesis, we are interested in the glueball with quantum numbers 0^{++}. Since these quantum numbers corrrespond to those of the vacuum, the vacuum contribution has to be subtracted from the operator, i.e.

$$\mathcal{O}_{0^{++}}(t) = \mathcal{O}_{0^{++}}(t) - \langle\Omega|\,\mathcal{O}_{0^{++}}(t)\,|\Omega\rangle\,. \tag{2.28}$$

For large t, the lowest glueball state dominates the correlation function, so that the energy E_G of the glueball in the representation $J^{PC} = 0^{++}$ can be extracted from the large time limit of $C(t)$.
The lowest-dimensional gauge-invariant gluon operators in the continuum look like $\mathrm{Tr}\,(F_{\mu\nu}F_{\rho\sigma})$, where $F_{\mu\nu}$ is the gauge field strength. From this, one can construct scalar, pseudoscalar and tensor operators with positive charge conjugation [17]. With the chromoelectric and chromo-

magnetic field given by $E_i = F_{i0}$ and $B_i = -\frac{1}{2}\epsilon_{ijk}F_{jk}$, a scalar operator can be written as

$$\mathcal{O}^B_{0^{++}}(x) = \mathrm{Tr}\,\vec{B}^2(x) \qquad \text{or} \qquad \mathcal{O}^E_{0^{++}}(x) = \mathrm{Tr}\,\vec{E}^2(x). \tag{2.29}$$

A lattice operator creating a state from the vacuum with quantum numbers of a glueball can be built from closed loops of link variables. These operators are gauge-invariant objects. Different definitions of lattice operators can be applied to ensure a good overlap with the state of interest [17]. In $SU(2)$, the simplest operator, which corresponds to the continuum operator $\mathcal{O}^B_{0^{++}}$ and creates the lowest glueball state 0^{++}, is

$$\mathcal{O}(t) = \mathrm{Re}\,\mathrm{Tr}\sum_{n\in L^3} U_{xy}(n,t) + U_{zx}(n,t) + U_{yz}(n,t). \tag{2.30}$$

It is constructed from the sum over all orientations of spatial plaquettes. By summing over all spatial lattice points, the glueball is projected to zero momentum.

2.4.3 Smearing

A problem one encounters when calculating masses via elementary loops on the lattice is that the overlap with the glueball state of interest becomes smaller when the lattice spacing is reduced. Decreasing the lattice spacing, the operator reduces in size while the physical wave function keeps its extension. Therefore, one needs operators with large overlap at small lattice spacings. In addition, the signal-to-noise-ratio gets worse at large times where we want to extract the energy of the lowest state. Thus, one needs operators for which the contributions from higher lying states are suppressed already for small temporal separations. A solution is the usage of non-local operators, which can be constructed in various ways.

Single-link smearing

The smearing applied to link variables exploited in the calculation of glueball operators uses single links and adds their staples with a weight factor λ_s, similar to APE-smearing [13]. This is performed iteratively, replacing $U_\mu^{N_s-1}$ in the N_s-th step by

$$\begin{aligned} U_\mu^{N_s}(n) =& U_\mu^{N_s-1}(n) \\ &+\lambda_s \sum_{\substack{\pm\nu \\ \mu\neq\nu\neq 0}} U_\nu^{N_s-1}(n) U_\mu^{N_s-1}(n+\hat{\nu}) U_\mu^{N_s-1}(n+\hat{\nu}+\hat{\mu}) U_\nu^{N_s-1\dagger}(n+\hat{\mu}). \end{aligned} \tag{2.31}$$

By choosing an appropriate weight factor λ_s and level of smearing steps N_s, the operator extends with a fine resolution over important scales.

Blocking

Another possibility to improve the signal-to-noise ratio and groundstate overlap for glueball operators is the *blocking* procedure. Variations of this method are also called *fuzzing* or *double-link smearing* [18]. It was introduced in [19].
Lattice gauge links are replaced by so-called *fuzzy superlinks* which extend over length $l_B = 2^{N_b}$, depending on the level of blocking, N_b. Those superlinks contain the direct path between two lattice sites separated by 2^{N_b} and a sum over elongated staples (see Fig. 2.2). In the N_b-th step

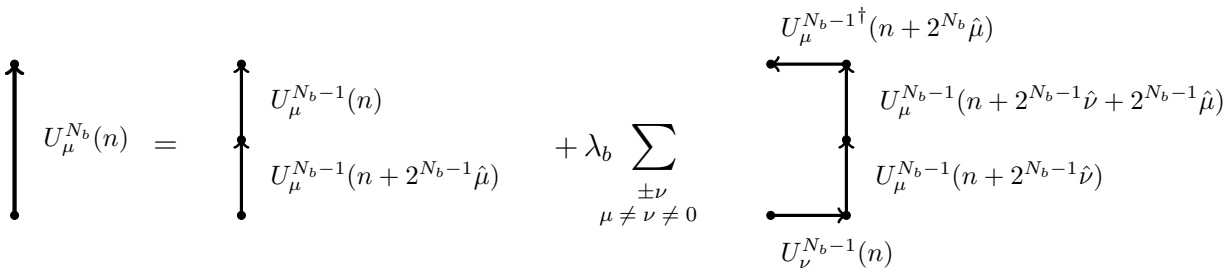

Figure 2.2: Illustration of blocking.

of blocking, the matrices are replaced by

$$\begin{aligned} U_\mu^{N_b}(n) =& U_\mu^{N_b-1}(n)U_\mu^{N_b-1}(n+2^{N_b-1}\hat{\mu}) \\ &+\lambda_b \sum_{\substack{\pm\nu \\ \mu\neq\nu\neq 0}} U_\nu^{N_b-1}(n)U_\mu^{N_b-1}(n+2^{N_b-1}\hat{\nu})U_\mu^{N_b-1}(n+2^{N_b-1}\hat{\nu}+2^{N_b-1}\hat{\mu})U_\nu^{N_b-1\dagger}(n+2^{N_b}\hat{\mu}). \end{aligned} \tag{2.32}$$

Finally, the new superlink is projected into $SU(N)$. There exist various versions of this blocking procedure, e.g. with additional diagonal staples [20].
Elementary loops calculated with blocked links now consist of a large number of original lattice links.
To hit the size of the glueball's wave function, the parameters N_b and λ_b have to be chosen suitably to be able to increase the operator overlap with the state of interest.

Blocking is faster than smearing, since the operator increases in each step by a factor of two, but the resolution is finer for smearing.
Both algorithms can be applied in a variety of combinations. When smearing link matrices that were blocked before, the algorithm in Equation (2.31) has to be adjusted in a straightforward way to be applicable to links of length l_B. In this work, we choose to first apply the single-link smearing to the original gauge links before the blocking procedure is performed.
In Section 5.1, we investigate which level of smearing and blocking is most suitable to minimize the effective mass of the lightest glueball which indicates less contributions from excited states. In this way, the groundstate mass can be identified at small temporal separations were the signal-to-noise ratio is still acceptable.

2.5 Lattice scale setting

Observables computed on the lattice are expressed in units of the lattice spacing and, thus, they are dimensionless. The correlation function is computed in terms of lattice points in temporal direction $t/a = n_t$ between the operators placed on the lattice. The value which we extract from the exponential decay,

$$C(n_t) \propto e^{-n_t am}, \tag{2.33}$$

is the dimensionless product of lattice spacing and mass, am. Any lattice observable can only be associated to a physical meaningful quantity if the lattice spacing a is known.
The lattice spacing can be determined by identifying a lattice quantity H with its physical

continuum equivalent H^{cont}. The choice of H, which defines the renormalization scheme, affects the lattice results. Consequently, the quantity should be precisely known experimentally and accurately computable on the lattice.
In the following, different renormalization schemes are introduced.

Scale setting using the string tension This renormalization scheme was one of the first methods used to set the scale [21]. By measuring the exponential decay of Wilson loops for large extensions, the dimensionless quantity $a^2\sigma$, where σ denotes the string tension, is extracted from the slope of the ordinary static potential at large distances. Then, this value is identified with the string tension σ^{cont} in the continuum. This renormalization scheme has some drawbacks as it requires the computation of large loops which is only possible up to limited numerical accuracy on fine lattices. Furthermore, it is not directly measurable in experiment.

Sommer scale The Sommer scale is derived in terms of the force between static quark and antiquark. Quantities are given in units of the length scale r_0 which is defined through

$$r^2 F(r)|_{r=r_c} = c \tag{2.34}$$

with $c = 1.65$ and $r_{1.65} = r_0$ being the common choice for r_c [22]. The length scale r_0 has a value of about 0.5 fm in QCD [23]. Finally, the lattice spacing can be found by extracting the parameters of the parametrization of the ordinary static potential Σ_g^+, $aV(r) = aV_0 - \alpha/r + a^2\sigma r$ in the region of r_0 and to calculate a from

$$a = r_0 \sqrt{\frac{a^2\sigma}{1.65 + \alpha}}. \tag{2.35}$$

The Sommer scale is a commonly used scale to determine the lattice spacing in Lattice QCD.
If one is interested in small distance aspects of pure gauge theory, the scale r_0 is inconvenient due to the increasing lattice size that is necessary for the static potential to reach the distance of r_0.
Therefore, a smaller reference length scale was introduced in [24]. Small separations were computed on fine lattices, whereas larger distances were evaluated on coarse lattices. In the overlap region, the reference length scale $r_c = 0.26$ fm with $c = 0.65$ is defined so that the scale can be set by relating r_0 to the new scale r_c. Using the equation defining r_c, one finds a/r_c and a/r_0 in the small and large distance region. The ratio is determined to $r_c/r_0 = 0.5133(24)$ in $SU(3)$ [24].

Scale setting via gradient flow The flow represents a smoothing in the gauge fields, which change according to a flow equation in flow time t. Measuring the quantity

$$F(t) = t^2 \langle E(t) \rangle , \tag{2.36}$$

with

$$E(t) = \frac{1}{4} F^a_{\mu\nu}(t) F^a_{\mu\nu}(t), \tag{2.37}$$

by computing Wilson loops with smoothed link variables, one can use $F(t)$ similar to the static force between two quarks to set the scale. The scale defining equations are

$$F(t)|_{t=t_0(c)} = c, \tag{2.38}$$

$$t\frac{d}{dt}F(t)|_{t=w_0^2(c)} = c. \tag{2.39}$$

For details see e.g. [25]. The advantage of this method is that no large distance computations are required. The scale setting can be performed on fine but small lattices [26].

Scale setting equation With data obtained in one of the existing scale setting procedures, one can perform a fit to derive a parametrization of the lattice spacing $a\,(\beta)$ for the determination of intermediate lattice spacings. For example, a polynomial fit was performed in [24] for $SU(3)$ in a large interval of lattice couplings derived from two reference scales r_0 and $r_{c=0.65}$. In [26] an interpolating polynomial of $\ln\left(t_0/a^2\right)$ for $SU(2)$ was derived from a scale setting procedure via the gradient flow reference scale t_0 in a lattice coupling range of $2.42 \leq \beta \leq 2.85$.

In order to specify a on fine lattices, we take a look at the renormalization equation in the weak-coupling limit. Note that a subscript on the lattice coupling β_{lat} is introduced in the following paragraph to avoid confusion with the β-function.
All bare parameters appearing in the theory have to be related to renormalized ones. The bare coupling g, which is related to the lattice coupling β_{lat} via $\beta_{\text{lat}} = 2N/g^2$, is the only bare parameter occuring in pure *SU(N)* gauge theory, it is related to the lattice spacing via the renormalization group equation

$$a\frac{\partial g}{\partial a} = \beta(g). \tag{2.40}$$

The weak-coupling expansion of the $\beta(g)$-function is given by [11]

$$\beta(g) = -\beta_0 g^3 - \beta_1 g^5 + \mathcal{O}(g^7), \tag{2.41}$$

with

$$\beta_0 = \frac{1}{(4\pi)^2}\left(\frac{11N}{3}\right), \tag{2.42}$$

and

$$\beta_1 = \frac{1}{(4\pi)^4}\left(\frac{34N^2}{3}\right). \tag{2.43}$$

The lattice spacing a in terms of the lattice coupling $\beta_{\text{lat}} = \frac{2N}{g^2}$ can be determined up to an integration constant by integrating the renormalization group equation (2.40) [21]. The leading order solution is

$$a\,(\beta_{\text{lat}}) = \frac{1}{\Lambda}\exp\left(-\frac{3\pi^2}{11}\beta_{\text{lat}}\right), \tag{2.44}$$

where Λ is used as reference to set the scale. Including the next-to-leading order term with the two-loop coefficient β_1 yields

$$a\,(\beta_{\text{lat}}) = \frac{1}{\Lambda}\left(\frac{\beta_{\text{lat}}}{4\beta_0}\right)^{\beta_1/2\beta_0}\exp\left(-\frac{3\pi^2}{11}\beta_{\text{lat}}\right). \tag{2.45}$$

β	2.50	2.70	2.85	3.00
a [fm]	0.0774	0.0408	0.0257	0.0165

Table 2.3: Lattice spacing estimates computed from the parametrization $a(\beta)$ derived from a scale setting via the gradient flow [26].

The third order result is given by

$$a\left(\beta_{\text{lat}}\right) = \frac{1}{\Lambda}\left(\frac{\beta_{\text{lat}}}{4\beta_0}\right)^{\beta_1/2\beta_0} \exp\left(-\frac{3\pi^2}{11}\beta_{\text{lat}}\right) \exp\left(-\frac{4c}{\beta_{\text{lat}}}\right), \tag{2.46}$$

with c being the third order loop expansion coefficient.
These equation can also serve as a parametrization of $a\left(\beta_{\text{lat}}\right)$ in the weak-coupling (large β_{lat}) regime. Λ has to be found through a fit to data for $a\left(\beta_{\text{lat}}\right)$. In the following, we omit the subscript on the lattice coupling β_{lat} again.

The parametrization derived from the gradient flow [26] provides a connection between a and β for large lattice couplings up to $\beta = 2.85$ and, correspondingly, small lattice spacings up to $a \approx 0.0257\,\text{fm}$. However, we want to compute even smaller distances, which correspond to larger lattice couplings. Exceeding the given range of validity and relying on the applicability of this parametrization also for larger couplings up to $\beta = 3.00$, a lattice spacing of $a(\beta = 3.00) \approx 0.0165\,\text{fm}$ is reached. Lattice spacings computed via the gradient flow scale setting equation at lattice couplings simulated in this thesis are given in Table 2.3, identifying $\sqrt{8t_0} \approx 0.30\,\text{fm}$ [26].
Using this parametrization possibly introduces systematic errors since a polynomial in β will not show the same behavior for very large β as the renormalization group equation in the weak-coupling limit (for large β) implies. To estimate those errors, different reasonable approaches are plotted in the region of larger lattice coupling in Figure 2.3.
The leading order solutions of the renormalization group equations (2.44) - (2.46) are fitted to the data points for $a(\beta)$ obtained from a scale setting via the Sommer scale in [27], where the same simulation algorithm was used as in this thesis. The renormalization group equation up to three loop order is fitted to all four available data points of $a(\beta)$ with the integration constant and the three loop coefficient as fit parameters. In contrast to the three loop order, the renormalization group equation solution at one and two loop order are not able to describe the data in the whole range or would need a second fit parameter. Thus, they are fitted to the data at $\beta = 2.60$ and 2.70.
The parametrization from scale setting via gradient flow and the third order renormalization group equation roughly coincide with the data in [27], when identifying $r_0 = 0.5\,\text{fm}$. However, both functions differ already at $\beta = 2.85$, where the polynomial fit should still be valid. While the renormalization group equation at three loop order lies below the gradient flow function, the estimate of the one or two loop order solution of the renormalization group equation lies higher. As a consequence, all estimates at large β are considered with caution. In Chapter 4, we compare the gradient flow scale setting estimates given in Table 2.3 to lattice spacings we determine via Equation (2.35) with our lattice data.

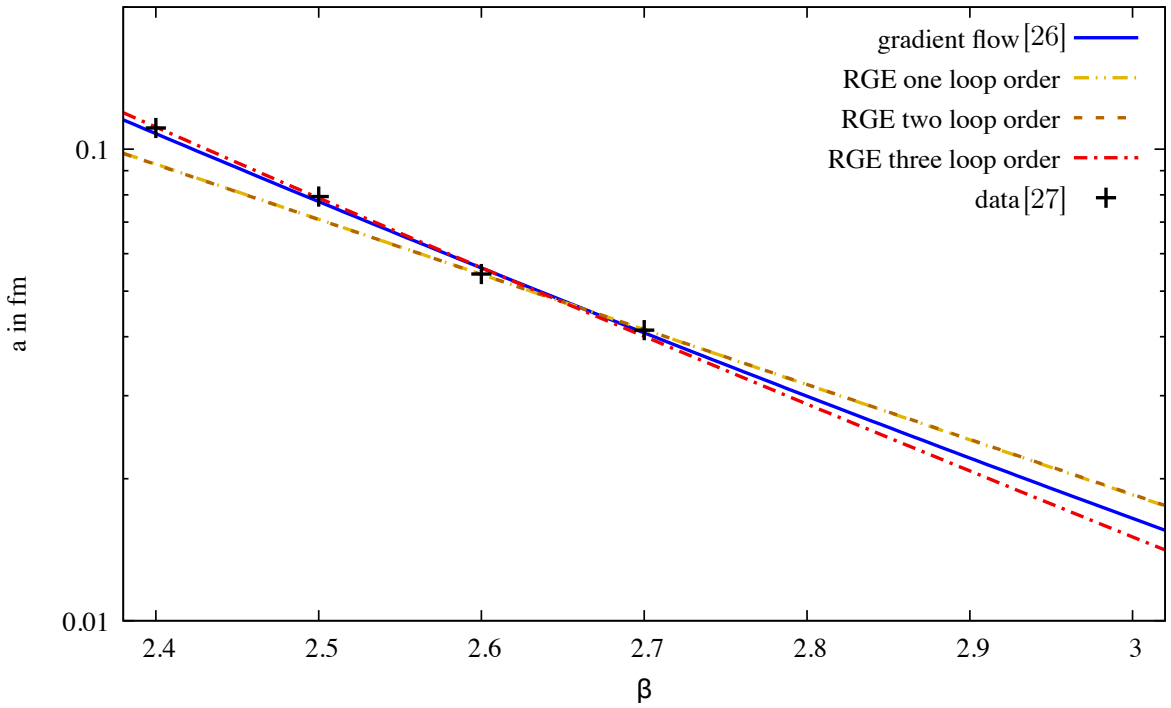

Figure 2.3: Different parametrizations of $a(\beta)$ with data points from the scale setting in [27] on a logarithmic scale. Renormalization group equation (RGE) solutions at one, two and three loop order are shown with dashed lines. The interpolating function from scale setting via gradient flow [26] is shown as a solid line.

3 Decay of excited static potentials into glueballs

In the following chapter, we investigate possible decays of hybrid static potentials. The gluonic field of a hybrid static potential is excited in contrast to the ordinary potential. At small quark-antiquark separations, the energy difference between hybrid and ordinary static potential is expected to increase. At some point the energy contained in the gluon field is sufficiently high to form a glueball such that the hybrid potential could dissolve into a glueball and the groundstate potential Σ_g^+. Then, an overlap of the hybrid static potential operator to the state consisting of Σ_g^+ and a glueball is energetically allowed. This will result in incorrect lattice results for hybrid static potentials.
In the following, we construct trial states for a combined state of the ordinary static potential and a glueball. In the course of this, we define a glueball state with appropriate properties under symmetry transformations of the dihedral group, the symmetry group of static potentials. Moreover, quantum numbers realized by the combination of static potential and glueball with angular momentum are discussed. We illustrate why some hybrid sectors are protected from a decay into the lightest glueball.
Furthermore, the quark-antiquark separations are determined at which hybrid static potentials reach the threshold energy to mix with a state of glueball and groundstate potential. This leads to a statement for the distance up to which lattice results for hybrid static potentials, which are obtained from an exponential fit to a single correlation function, are trustworthy.

3.1 Direct product representations

First of all, the combined quantum numbers of the glueball and groundstate static potential are discussed.
Generally speaking, the quantum numbers of decay products must add up to the quantum numbers of the decaying state, the hybrid static potential. If a hybrid static potential which has an angular momentum with respect to the separation axis, Λ, decays into the ordinary static potential Σ_g^+ with zero angular momentum and a glueball, the glueball has to carry this orbital angular momentum, $L_z = \Lambda$. Moreover, the groundstate static potential Σ_g^+ can only be joined by a glueball state with quantum numbers identical to the hybrid static potential. Thus, the glueball state is in a representation of the symmetry group of static potentials, the dihedral group. The construction of this trial state from a glueball with quantum numbers J^{PC} is presented in the following section.
The direct product table of irreducible representations in the dihedral group, given in Table 3.1, indicates which combination of decay products in representations of $D_{\infty h}$ resemble hybrid quantum numbers.

$R^q \times R^p$	Σ^+	Σ^-	Π	Δ
Σ^+	Σ^+	Σ^-	Π	Δ
Σ^-		Σ^+	Π	Δ
Π			$\Sigma^+ + \Sigma^- + \Delta$	$\Pi + \Phi$
Δ				$\Sigma^+ + \Sigma^- + \Gamma$

Table 3.1: Direct product table of irreducible representations for the infinite dihedral group up to $\Lambda = 2$. The table is symmetric. Quantum number $\eta = g, u$ is omitted here. Obviously, $g \times u = u$, $u \times u = g$ and $g \times g = g$.

We consider the product of a static potential in the representation R^q with a glueball state transforming as the irreducible representation R^p. In general, the representation generated by a product of two irreducible representations is reducible. However, the product of an irreducible representation R^p with the trivial representation Σ_g^+ yields the irreducible representation R^p itself. Thus, the product state of a glueball and the ordinary static potential Σ_g^+ transforms according to the representation of the glueball state $R^p = L_z{}^{\epsilon}_{\eta}$.
When considering a hybrid static potential as a decay product, one has to take a look at the multiplication table 3.1. High lying hybrid potentials could also decay into Π_u and a glueball state transforming as the appropriate representation if their energy is sufficiently high. But, when decay products are a combination of two non-trivial irreducible representations, the result belongs to a reducible representation and would contribute to more than one channel.

In the following, operators for the decay products are constructed. On this basis, hybrid static potentials can be identified which are excluded from a decay into the lightest glueball.

3.2 Operator of decay states

To start with, we note that the simple operator $\mathcal{O}_{\Sigma_g^+}$ creating the ordinary static potential trial state, as presented in Equation (2.16), is invariant under rotations, parity and charge conjugation transformations as well as reflection $\mathcal{P}_x$. It is obviously in the trivial representation Σ_g^+ of $D_{\infty h}$.

Next, we consider the simplest creation operator for the lowest mass glueball

$$\mathcal{O}_{\text{glueball}}(x) = Tr\vec{B}^2(x). \tag{3.1}$$

It creates a glueball with quantum numbers $J^{PC} = 0^{++}$ from the vacuum. This operator is rotationally invariant. But, we can construct the operator

$$\mathcal{O}_{L_z\eta} = \int \mathrm{d}^3r \; e^{iL_z\varphi} f(z,r) \; \mathcal{O}_{\text{glueball}}(r,\varphi,z), \tag{3.2}$$

where d^3r denotes the three-dimensional volume element in cylindrical coordinates and $f(r,z)$ serves as a distribution function placing the glueball along z and r. In contrast to the simple rotationally invariant glueball operator, it has angular momentum L_z with respect to the z-axis.

This is demonstrated by rotating the operator by an angle α

$$\begin{aligned} R(\alpha)\mathcal{O}_{L_z\eta}R^\dagger(\alpha) &= \int \mathrm{d}^3r\ e^{iL_z\varphi} f(z,r)\mathcal{O}_{\text{glueball}}(r,\varphi+\alpha,z) \\ &= e^{-i\alpha L_z}\int \mathrm{d}^3r\ e^{iL_z\varphi} f(z,r)\mathcal{O}_{\text{glueball}}(r,\varphi,z). \end{aligned} \tag{3.3}$$

The operator creates a trial state which is an eigenstate of the angular momentum operator with eigenvalue L_z. Furthermore, each value of orbital angular momentum along z can be implemented by setting the weight factor $e^{iL_z\varphi}$.

It can be shown that the state given by Equation (3.2) has definite quantum number η, when an appropiate function $f(r,z)$ with the following property under parity transformation is chosen:

$$f(r,z) \xrightarrow{\mathcal{P}} f(r,-z) = (-1)^f f(r,z). \tag{3.4}$$

Then, the parity transformation and charge conjugation of the operator yield

$$\begin{aligned} \mathcal{P}\circ\mathcal{C}\left[\mathcal{O}_{L_z\eta}\right] &= \mathcal{P}\circ\mathcal{C}\left[\int \mathrm{d}^3r\ e^{iL_z\varphi} f(r,z)\ \mathcal{O}_{\text{glueball}}(r,\varphi,z)\right] \\ &= \mathcal{C}\left[\int \mathrm{d}^3r\ e^{iL_z\varphi} f(r,z)\ \mathcal{O}^{\mathcal{P}}_{\text{glueball}}(r,\varphi+\pi,-z)\right] \\ &= \mathcal{C}\left[\int \mathrm{d}^3r\ e^{iL_z(\varphi-\pi)} f(r,-z)\ \mathcal{O}_{\text{glueball}}(r,\varphi,z)\right] \\ &= e^{-iL_z\pi}(-1)^f \int \mathrm{d}^3r\ e^{iL_z\varphi} f(r,z)\ \mathcal{O}^{\mathcal{C}}_{\text{glueball}}(r,\varphi,z) \\ &= e^{-iL_z\pi}(-1)^f \int \mathrm{d}^3r\ e^{iL_z\varphi} f(r,z)\ (-1)^2\mathcal{O}_{\text{glueball}}(r,\varphi,z) \\ &= (-1)^{L_z+f}\,\mathcal{O}_{L_z\eta}. \end{aligned} \tag{3.5}$$

Here, it was used that the chromomagnetic field $\vec{B}$ appearing in the 0^{++}-glueball operator has positive parity and the minus sign occuring due to charge conjugation cancels due to the square. The eigenvalue of the operator with respect to $\mathcal{P}\circ\mathcal{C}$ is $\eta = (-1)^{L_z+f}$.

The properties of the glueball state under inversion of the x-axis, $\mathcal{P}_x$, can be seen by applying the transformation to Equation (3.2) given that an inversion of the x-axis yields $\varphi \xrightarrow{\mathcal{P}_x} \pi-\varphi$:

$$\begin{aligned} \mathcal{P}_x\left[\mathcal{O}_{L_z\eta}\right] &= \mathcal{P}_x\left[\int \mathrm{d}^3r\ e^{iL_z\varphi} f(r,z)\ \mathcal{O}_{\text{glueball}}(r,\varphi,z)\right] \\ &= \int \mathrm{d}^3r\ e^{iL_z\varphi} f(r,z)\ \mathcal{O}_{\text{glueball}}(r,\pi-\varphi,z) \\ &= \int \mathrm{d}^3r\ (-1)^{L_z} e^{-iL_z\varphi} f(r,z)\ \mathcal{O}_{\text{glueball}}(r,\varphi,z). \end{aligned} \tag{3.6}$$

It can be seen from above that this state is no $\mathcal{P}_x$ eigenstate for arbitrary angular momentum L_z because the weight factor changes, $e^{iL_z\varphi} \xrightarrow{\mathcal{P}_x} (-1)^{L_z}e^{-iL_z\varphi}$. Only the operator with $L_z = 0$ is already an eigenstate with eigenvalue $\epsilon = +$.
A trial state with definite quantum number ϵ can be constructed by projecting the state given in (3.2) onto an eigenstate of the operator $\mathcal{P}_x$. The projection operator is

$$\mathbb{P}_{P_x} = \frac{1}{2}\left(1+\epsilon\mathcal{P}_x\right). \tag{3.7}$$

Hence, a glueball trial state with definite angular momentum along the z-axis, L_z, behavior under combined parity and charge conjugation, η, and inversion of an axis perpendicular to the

z-axis, ϵ, is created by

$$\mathcal{O}_{L_{z\eta}^{\epsilon}} = \frac{1}{2}\left(1+\epsilon\mathcal{P}_x\right)\int \mathrm{d}^3r\; e^{iL_z\varphi} f(r,z)\; \mathcal{O}_{\text{glueball}}(r,\varphi,z). \tag{3.8}$$

To conclude, an irreducible tensor operator $\mathcal{O}_{L_{z\eta}^{\epsilon}}$ was constructed that transforms according to the irreducible representation $\Lambda_\eta^\epsilon = L_{z\eta}^{\epsilon}$ of the infinite dihedral group $D_{\infty h}$ for all symmetry transfomations of the group. According to the Wigner-Eckart theorem, the tensor operator creates a trial state with quantum numbers $L_{z\eta}^{\epsilon}$ when acting on the vacuum.

Now, glueball and groundstate static potential operators can be combined to construct a state which has quantum numbers identical to a hybrid static potential. Such a creation operator is given by

$$\begin{aligned}\mathcal{O}_{\Sigma_g^+ + \text{glueball}} &= \mathcal{O}_{\Sigma_g^+} \times\; \mathcal{O}_{L_{z\eta}^{\epsilon}} \\ &= \bar{q}(\vec{x}-r'/2\hat{e}_z)U(\vec{x}-r'/2\hat{e}_z,\vec{x}+r'/2\hat{e}_z)q(\vec{x}+r'/2\hat{e}_z)\times \\ &\quad \int \mathrm{d}^3r\; \frac{1}{2}\left(1+\epsilon\mathcal{P}_x\right) e^{iL_z\varphi} f(z,r)\; \mathcal{O}_{\text{glueball}}(r,\varphi,z).\end{aligned} \tag{3.9}$$

3.2.1 Possible quantum numbers

Quantum numbers $L_{z\eta}^{\epsilon}$, which one can generate through the construction of an operator of the form (3.8), are determined by the choice of glueball operator $\mathcal{O}_{\text{glueball}}$ with its transformation properties. The distribution function $f(r,z)$, its behavior under parity, f, and angular momentum L_z can be chosen appropriately to create the desired quantum numbers.
In Table 3.2, we list the possible choices and the resulting quantum numbers $L_{z\eta}^{\epsilon}$ in the rightmost column.

It is important to note that with a 0^{++}-glueball only operators with non-zero angular momentum L_z can be constructed to have arbitrary quantum number ϵ. The reason is explained in the following.
Under inversion of the x-axis, the weight factor changes, $e^{iL_z\varphi} \xrightarrow{\mathcal{P}_x} (-1)^{L_z} e^{-iL_z\varphi}$. The glueball operator $\mathcal{O}_{0^{++}}(x) = \operatorname{Tr}\vec{B}^2(x)$ itself does not change under action of $\mathcal{P}_x$. For that reason, the parity transformed operator with $L_z = 0$ equals the original state because the weight factor is always $e^{i\varphi L_z} = 1$. Hence, states with $L_z = 0$ have definite $\epsilon = +$ but the quantum number $\epsilon = -$ is not accessible through the combination of the ordinary static potential and a 0^{++}-glueball with zero angular momentum $L_z = 0$.
Instead of the 0^{++}-glueball, hybrid potentials with $\Lambda = 0$ and $\epsilon = -$ could decay into the ordinary static potential and a glueball with higher mass and different quantum numbers, if the necessary energy would be reached. For example, a glueball having non-zero spin like the second lightest 2^{++} could be combined with the ordinary static potential to yield any of the hybrid quantum numbers. Another option is a glueball with negative parity $P = -$, like the third lightest 0^{-+}-glueball. With this choice, the final operator can only have definite $\epsilon = -$ if the angular momentum with respect to the separation axis is zero, $L_z = 0$.

L_z	$(-1)^f$	$\eta = (-1)^{L_z+f}$	ϵ	$L_{z\eta}^{\epsilon}$
0	-1	-1	$+1$	Σ_u^+
0	$+1$	$+1$	$+1$	Σ_g^+
1	-1	$+1$	$+1$	Π_g^+
1	-1	$+1$	-1	Π_g^-
1	$+1$	-1	$+1$	Π_u^+
1	$+1$	-1	-1	Π_u^-
2	-1	-1	$+1$	Δ_u^+
2	-1	-1	-1	Δ_u^-
2	$+1$	$+1$	$+1$	Δ_g^+
2	$+1$	$+1$	-1	Δ_g^-

Table 3.2: Possible quantum numbers $L_{z\eta}^{\epsilon}$ of states created by the operator given in Equation (3.9) with a 0^{++}-glueball.

Although, other hybrid quantum numbers can be realized with glueballs having spin, the necessary energy for a decay of a hybrid into such a glueball increases and decays are prohibited energetically up to very small separations. The necessary threshold for a decay of a hybrid potential into the ordinary static potential accompanied by a 0^{++}- or 2^{++}-glueball is discussed later.

3.3 Momentum projection

A glueball rotating with angular momentum L_z with respect to the z-axis has momentum which increases its energy. But we are interested in the lowest energy of the state containing the ordinary potential and the glueball. Consequently, we look for an operator which, on the one hand, has definite angular momentum creating quantum numbers $L_{z\eta}^{\epsilon}$ similar to a hybrid static potential but on the other hand, has zero or at least low momentum $\vec{p}$.

To project an operator $\mathcal{O}(\vec{x})$ to definite momentum, a Fourier transform is performed

$$\tilde{\mathcal{O}}(\vec{p}) = \frac{1}{V}\int_V \mathrm{d}^3x\ \mathcal{O}(\vec{x})\ e^{-i\vec{p}\vec{x}}. \tag{3.10}$$

The plane wave $e^{-i\vec{p}\vec{x}}$ is a solution of the Schrödinger equation for a free particle (see Appendix A.1). It can be expanded in terms of cylindrical waves, which is shown in detail in Appendix A.2.
Inserting the cylindrical wave expansion of plane waves (A.17) yields

$$\tilde{\mathcal{O}}(\vec{p}) = \frac{1}{V}\int_V \mathrm{d}^3x\ \mathcal{O}(\vec{x})\, e^{-ip_z z} \sum_{m=-\infty}^{\infty} (-i)^m J_m(pr) e^{-im(\varphi-\varphi_p)}. \tag{3.11}$$

$J_m(pr)$ are Bessel functions and the momentum vector is separated into the transverse momentum $\vec{p}_\perp = (p, \varphi_p)$ and the momentum along z, p_z.

In most cases, creation operators are projected to zero momentum. Choosing $p = 0$, the Bessel function has a zero argument and vanishes for all values of $m > 0$ (cf. Equation (A.13)). Hence, the only contribution in the zero-momentum operator comes from an operator with vanishing angular momentum. For non-zero momentum, an infinite number of terms with different angular momentum m along the z-axis contribute to the plane wave expansion and consequently to the momentum projected operator in Equation (3.11).
However, we consider glueball states with definite angular momentum. Making use of the inverse Fourier transform of the glueball operator and the cylindrical wave expansion, we can write the operator $\mathcal{O}_{L_z}(r, z)$ with definite angular momentum as

$$\mathcal{O}_{L_z}(r,z) = \int \mathrm{d}\varphi\, e^{iL_z\varphi}\, \mathcal{O}_{\text{glueball}}(r,\varphi,z) \tag{3.12}$$

$$= \int \mathrm{d}\varphi\, e^{iL_z\varphi} \left(\frac{1}{2\pi} \int \mathrm{d}^3p\, \mathcal{O}_{\text{glueball}}(p,\varphi_p,p_z) e^{i\vec{p}\vec{r}} \right) \tag{3.13}$$

$$= \int \mathrm{d}\varphi\, e^{iL_z\varphi} \sum_{m=-\infty}^{\infty} \frac{1}{2\pi} \int \mathrm{d}^3p\, \mathcal{O}_{\text{glueball}}(p,\varphi_p,p_z)\, i^m J_m(pr) e^{im(\varphi-\varphi_p)} e^{ip_z z}. \tag{3.14}$$

With $\int \mathrm{d}\varphi\, e^{i\varphi(m+L_z)} = 2\pi\delta_{m(-L_z)}$ and $J_{-m}(pr) = (-1)^m J_m(pr)$, this yields

$$\mathcal{O}_{L_z}(r,z) = i^{-L_z} \int \mathrm{d}^3p\, \mathcal{O}_{\text{glueball}}(p,\varphi_p,p_z) J_{-L_z}(pr)\, e^{iL_z\varphi_p} e^{ip_z z} \tag{3.15}$$

$$= i^{L_z} \int \mathrm{d}^3p\, \mathcal{O}_{\text{glueball}}(p,\varphi_p,p_z) J_{L_z}(pr)\, e^{iL_z\varphi_p} e^{ip_z z}. \tag{3.16}$$

Thus, an infinte number of momentum values contributes to an operator with definite angular momentum L_z.
As a result, operators can, in general, be constructed to have either definite momentum p or definite angular momentum L_z. Except for states without angular momentum, $L_z = 0$, which can be projected to vanishing momentum.

3.4 Decay threshold

If the energy of the hybrid static potential is sufficiently high, it can decay into its groundstate and a glueball. The operator used to compute a hybrid static potential on the lattice will have non-zero overlap with such a decay state yielding inaccurate results for the hybrid potential. The aim is to determine the separation distance beyond which lattice results of hybrid static potentials can be trusted or if they are contaminated by the contribution of a decay state containing the ordinary static potential and a glueball. So, we take a look at the energy needed for a decay and determine the separation for hybrid static potentials below which they exceed this energy threshold. To estimate this, we consider precise results for hybrid static potentials in different channels from an elaborate study in $SU(3)$ [7].

The glueball accompanying the ordinary static potential between the quark-antiquark pair in a finite volume has mass m and momentum $\vec{p}$, which is discretized on a lattice with spatial volume L^3 according to $\vec{p} = \frac{2\pi}{L}(n_x, n_y, n_z),\ n_i \in \mathbb{Z}$.
The energy of the state is given by the energy of the ordinary static potential depending on r,

$V_{\Sigma_g^+}(r)$, and the mass and momentum of the glueball, m and $\vec{p}$,

$$E = V_{\Sigma_g^+}(r) + \sqrt{m^2 + \vec{p}^2}. \tag{3.17}$$

If $\vec{p} = 0$, the glueball state can only have zero angular momentum L_z with respect to the z-axis following Section 3.3. In this case, the energy added to the ordinary potential is given by the mass of the glueball.
For angular momentum L_z different from zero, the glueball has to carry some momentum $p \neq 0$ in the xy-plane. The minimal momentum in a finite volume with periodic boundaries is $p = \frac{2\pi}{L}$. To get an estimate of the separation distance where the minimum threshold energy is reached, we consider the lowest possible energy of a glueball with non-zero momentum,

$$E_{\text{glueball}} = \sqrt{m^2 + \left(\tfrac{2\pi}{L}\right)^2}. \tag{3.18}$$

Due to the inverse dependence on the finite volume size L, the threshold becomes larger for small box sizes and smaller for large volume lengths.

Figures 3.1 - 3.2 illustrate the threshold energies. Data points denote lattice potential results from [7]. Moreover, Σ_g^+, Π_u and Σ_u^- are shown together with a parametrization also derived in [7].

Based on Table 3.2, hybrid static potential Σ_u^+ can decay into ordinary static potential Σ_g^+ and the lightest glueball with zero orbital angular momentum $L_z = 0$. In this case, the glueball state has zero momentum, $p = 0$. Hence, a decay of Σ_u^+ into the lightest glueball is possible when its energy exceeds the energy of the ordinary static potential and the glueball mass of $m_{0^{++}} \approx 4.21/r_0$ [28], $V_{\Sigma_g^+}(r) + m_{0^{++}}$. This is illustrated in Figure 3.1a. The necessary energy is plotted as a dashed line.
It can be seen that the hybrid potential Σ_u^+ has enough energy for a decay into a zero-momentum glueball already at relatively large quark-antiquark separations, $r_{\text{crit}} \approx 0.9 r_0$. The first excitation of the ordinary static potential, $\Sigma_g^{+\prime}$, also displayed in Figure 3.1a, exceeds the threshold energy for a decay at a distance of $r_{\text{crit}} \approx 0.4 r_0$.

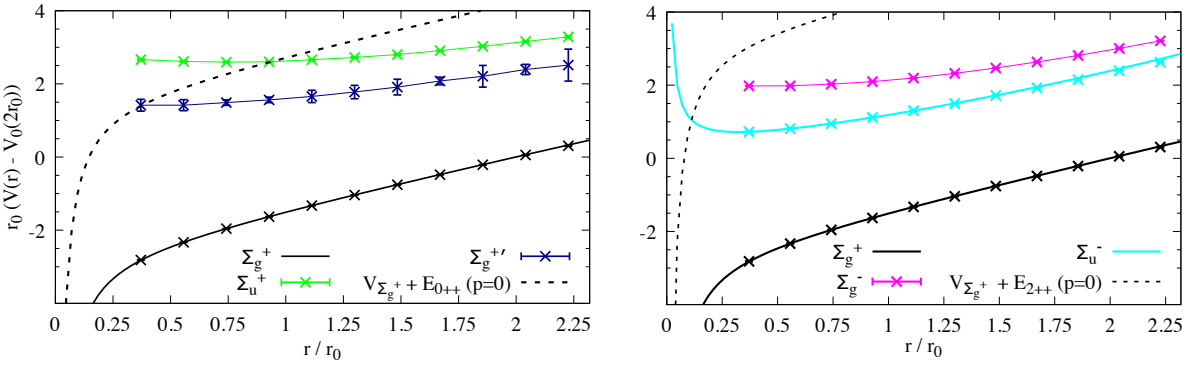

(a) Σ_u^+, $\Sigma_g^{+\prime}$ (b) Σ_u^-, Σ_g^-

Figure 3.1: Lattice data for excited static potentials. Dashed lines represent the energy of a combination of ordinary static potential with an additional zero-momentum glueball $V_{\Sigma_g^+} + E_{\text{glueball}}(p = 0)$. Glueball 0^{++} in the left plot, 2^{++} on the right hand side.

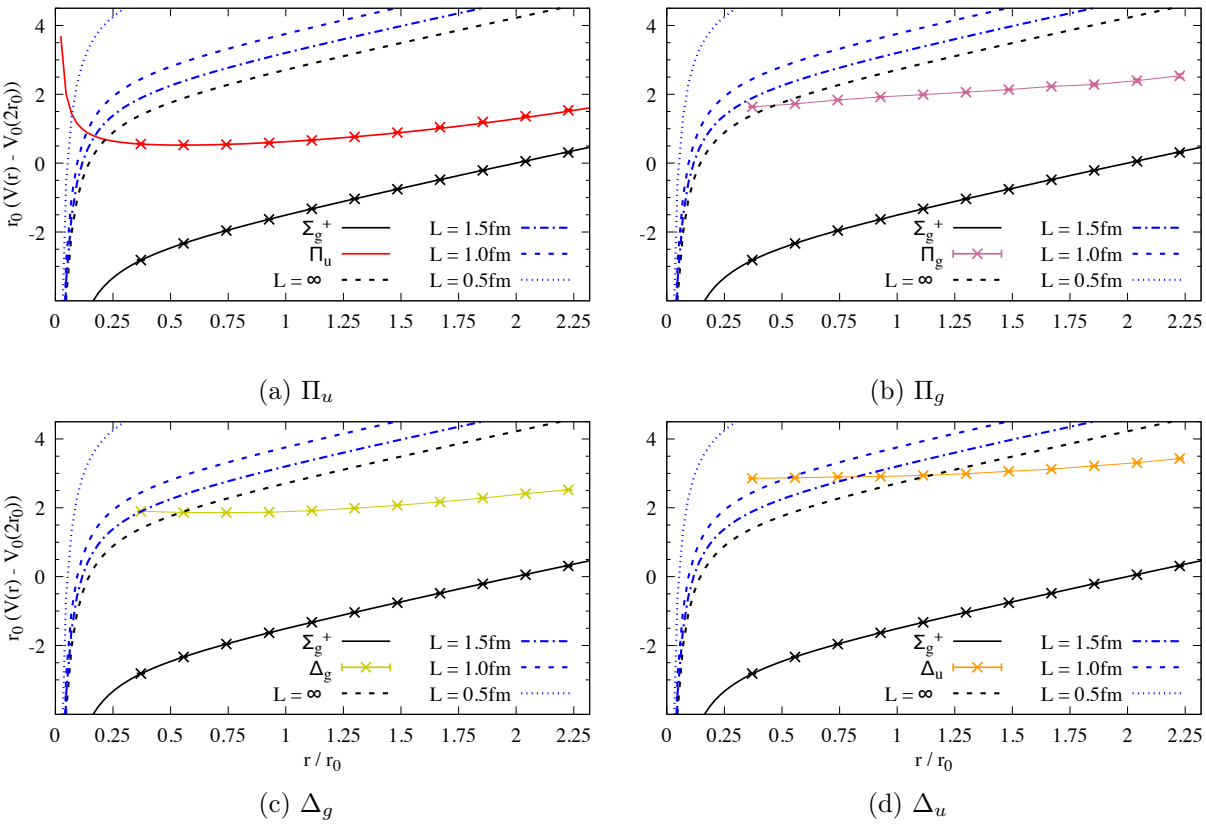

(a) Π_u (b) Π_g

(c) Δ_g (d) Δ_u

Figure 3.2: Lattice data for hybrid static potentials. Dashed lines represent the energy of a combination of ordinary static potential with an additional nonzero-momentum glueball $V_{\Sigma_g^+}(r) + \sqrt{m_{0^{++}}^2 + p^2}$ depending on different volume lengths $L = 0.5,\ 1.0,\ 1.5\,\mathrm{fm}$ and $L = \infty$ corresponding to vanishing momentum $p = 0$.

According to Section 3.2.1, a hybrid potential with quantum numbers $L_z = 0$ and $\epsilon = -$ cannot decay into a glueball with quantum numbers 0^{++} and the ordinary static potential. This applies to Σ_u^- and Σ_g^-. They can decay into 2^{++}- or 0^{-+}-glueball. Since these glueballs are heavier than 0^{++}, the threshold is higher. In Figure 3.1b, the threshold is shown as a dashed line for the next lightest glueball 2^{++} which has a mass of $m_{2^{++}} \approx 5.85/r_0$ [28].
The threshold is not reached until very small separations, $r_{\mathrm{crit}} \approx 0.1 r_0$ for Σ_u^- and $r_{\mathrm{crit}} < 0.25 r_0$ for Σ_g^-. Therefore, a decay of Σ_u^- and Σ_g^- does not concern the results for hybrid static potentials at quark-antiquark separations computed in [7].

Figure 3.2 shows hybrid static potentials and thresholds for a decay into a non-zero momentum 0^{++}-glueball depending on different lengths of finite volume, $L = 0.5,\ 1.0,\ 1.5\,\mathrm{fm}$ and infinite volume $L = \infty$, which corresponds to $p = 0$. Here, one can read off the critical separations where a decay into the ordinary static potential and a glueball becomes possible.
Π_u is shown with a parametrization derived in [7]. It is the lowest hybrid static potential, hence, one has to go to very short separations of $r_{\mathrm{crit}} < 0.2 r_0$ to exceed the threshold energy for a decay. For a decay into a glueball with higher momentum and in a smaller finite volume, the distance has to be decreased even further.
Π_g has not enough energy for a decay into a glueball in a large finite volume above $r_{\mathrm{crit}} \approx 0.5 r_0$. Other hybrid static potentials lie higher so that some of them exceed the threshold energy at relatively large separations and small L.

Λ_η^ϵ	Π_u	Π_g	Δ_g	Δ_u	$\Sigma_g^{+\prime}$	Σ_u^+	Σ_u^-	Σ_g^-
r_{crit}/r_0	0.2	0.5	0.5	1.1	0.4	0.9	0.1	0.25

Table 3.3: Largest approximate separation distance r_{crit} of hybrid static potentials Λ_η^ϵ below which lattice results might be contaminated due to a decay into a glueball and the ordinary static potential Σ_g^+. For Π_u, Π_g, Δ_g and Δ_u, the estimate of r_{crit} is given for the case of an infinite volume $L \to \infty$ (for details see the discussion).

Δ_g reaches the threshold energy at $r_{\text{crit}} \approx 0.4 r_0$ for a finite volume size of $L = 1.5\,\text{fm}$, whereas one would have to go to very short quark-antiquark distances to attain the threshold for a very small volume of length $L = 0.5\,\text{fm}$.
The same observation can be made for hybrid static potential Δ_u, it exceeds the threshold energy for a volume size of $L = 1.5\,\text{fm}$ at $r_{\text{crit}} \approx 0.8 r_0$ and for volume with length $L = 1\,\text{fm}$ at $r_{\text{crit}} \approx 0.5 r_0$.

In conclusion, according to the evaluation carried out in this section, the lowest hybrid static potential has not enough energy for a glueball decay at separations computed in [7]. However, due to the small lattice spacings studied in this thesis, we get close to the critical distance where the minimal threshold energy is reached, even with the very small lattice volume.
The second lowest hybrid static potential Σ_u^- is not affected by a decay into the lightest glueball. On the contrary, the energy of other hybrid static potentials, in particular, higher lying potentials like Σ_u^+, Δ_g and Δ_u, is sufficient for a decay into the lightest glueball with low momentum at commonly computed separation distances. Therefore, results from large finite volumes and at small quark-antiquark distances, which are below the estimates given in Table 3.3, should be treated with caution due to a possible decay.
The contamination of lattice results can be avoided by including the operator for the combined trial state of glueball and ordinary static potential in the analysis (cf. Section 3.2). The computation of a correlation matrix of operators for the hybrid potential and the combined state of glueball and groundstate potential will help to extract accurate lattice results for the hybrid potential. As a preparation for this study, the computation of static potentials and the lightest glueball at small lattice spacings is investigated separately in the final part of this thesis.

Part II

Lattice results

4 Static potentials at small lattice spacings

The ordinary static potential Σ_g^+ together with the lowest hybrid static potential Π_u is computed in $SU(2)$ pure gauge theory on four lattice ensembles with different lattice couplings β. Lattice parameters are presented in Table 4.1. The lattice volume $(T/a) \times (L/a)^3$ is chosen such that the spatial extent in physical units is $L > 0.5\,\mathrm{fm}$.
Gauge field configurations are obtained with a Monte Carlo heatbath algorithm with Wilson plaquette action (see Chapter 2). Thermalization and autocorrelation time are checked with the plaquette variable for each ensemble. Finally, measurements are performed on N_{meas} configurations, which are separated by 100 Monte Carlo updates and also binned to ensure that results are mostly uncorrelated.
In the end, statistical errors for all observables are determined via a jackknife analysis, which is explained in Section 2.2.

Wilson loops (2.17) and (2.27) are computed from APE-smeared gauge links. Furthermore, they are averaged over all lattice sites and all three spatial directions. Finally, we compute the effective potential

$$aV_{\mathrm{eff}}(r,t) = \ln\left(\frac{W(r,t)}{W(r,t+a)}\right). \tag{4.1}$$

The large time limit of this function is given by the potential $aV(r)$ which is commonly extracted by fitting a constant to the effective potential at large t/a. Since excited states still contribute to the effective potential at the measured temporal separations, we also perform a least squares fit with the three-parameter function, which contains exponential contributions from excited states,

$$aV_{\mathrm{eff}}(r,t) = aV(r) + C(r)\exp(-\Delta V(r)t), \tag{4.2}$$

with aV, C and ΔV as fit parameters.

4.1 Ordinary static potential Σ_g^+

The ordinary static potential Σ_g^+ between a static quark and antiquark is an observable that is simple to compute on the lattice. Parallel to the hybrid static potential, the groundstate

β	$(T/a) \times (L/a)^3$	N_{meas}
2.50	48×24^3	2520
2.70	48×24^3	1000
2.85	48×26^3	2520
3.00	48×34^3	2390

Table 4.1: Lattice ensembles.

is computed on all lattice ensembles. As will be discussed in the following, difficulties in the computation of static potentials ocurring at small lattice spacings are already indicated in the analysis of the groundstate potential. Furthermore, the ordinary static potentials obtained from different lattices serve as the basis for the subtraction of the static quark self-energy which is distinct for each lattice ensemble.
In Figure 4.1, we present the effective potentials computed at $\beta = 2.50$, 2.70, 2.85 and 3.00 in lattice units at temporal separations $t = 1a \dots 11a$ in separate plots. From these plots, we see that the signal-to-noise ratio for larger lattice spacing decreases faster with t/a. The growth of noise is expected because the separation in physical units t is much larger than on fine lattices. For the smallest lattice spacing, which corresponds to the largest coupling $\beta = 3.00$, it already gets difficult to extract the plateau for the ordinary potential. This is illustrated in Figure 4.2, where $V_{\text{eff}}(r = 6a, t)$ is shown exemplarily for $\beta = 2.50$ and $\beta = 3.00$. Whereas one can identify a plateau in the lattice data of the effective potential at lattice coupling $\beta = 2.50$ before the signal is hidden by noise, the effective potential derived at $\beta = 3.00$ seems to not reach a plateau at the computed temporal separations. Comparing the temporal separation in physical units, the plateau at small β is identified at $t \approx 0.5\,\text{fm}$, whereas $aV_{\text{eff}}(r/a, t)$ at $\beta = 3.00$ is only computed up to $t \approx 0.17\,\text{fm}$.
As a result, the fit estimate of the potential value could be too high. Probably, the temporal separation in physical units is not large enough so that the effective potential, in particular at larger r/a, is still dominated by excited states. Since this difficulty appears already for the simpler observable, it is expected to be a main problem in the analysis of hybrid static potential. This will be discussed in the following section.
To compensate this adverse effect at small lattice spacings, we perform a three-parameter fit with Equation (4.2) which contains a term for the contribution of higher states. This yields reasonable results for the ordinary static potential.

The final results from fitting the effective potentials for the ordinary static potentials, $aV_{\Sigma_g^+}(r/a)$, are shown in Figure 4.3 for each ensemble separately. Results from different fits are compared. It can be seen at larger r/a that results extracted via fitting a plateau lie slightly higher than the value obtained from the fit of Equation (4.2). Here, it is obvious that the plateau fits overestimate the potential value $aV(r/a)$, therefore, we consider the results from the three-parameter fit for the ordinary static potential in the following.
At small β, which corresponds to large lattice spacings, the static potential shows the linear rise which is expected at such physical distances. At large β, i.e. small lattice spacings, the attractive $1/r$-like behavior is visible.

The lattice data can be parametrized with the Cornell potential given by Equation (2.12). A least squares fit between $r = 2a$ and $12a$ at each lattice ensemble yields the parameters listed in Table 4.2.

Lattice spacing The lattice spacing can be determined through the fit parameters according to Equation (2.35). Results are also listed in Table 4.2.
For better comparison to the other lattice spacing estimates at large β, we add our results to Figure 2.3 shown in Section 2.5. This is shown in Figure 4.4. Our estimates of $a(\beta = 2.50)$

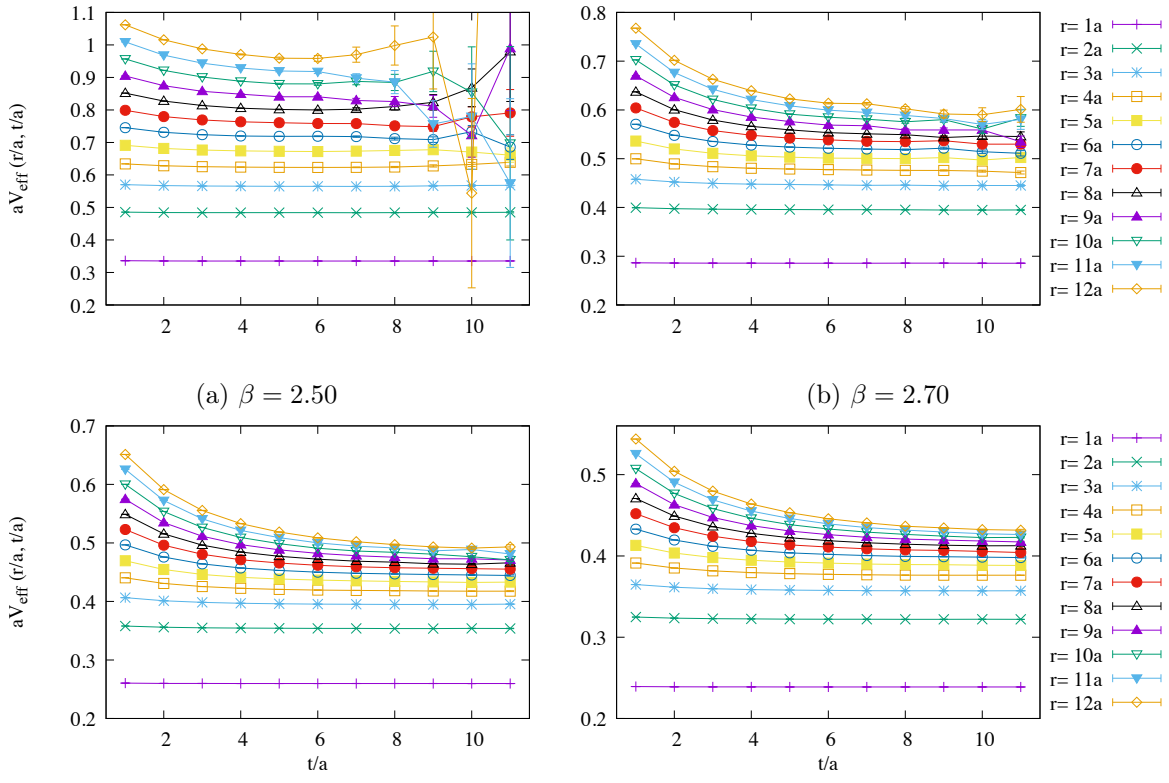

(a) $\beta = 2.50$ (b) $\beta = 2.70$

(c) $\beta = 2.85$ (d) $\beta = 3.00$

Figure 4.1: Effective potentials $aV_{\text{eff}}(r,t)$ for Σ_g^+.

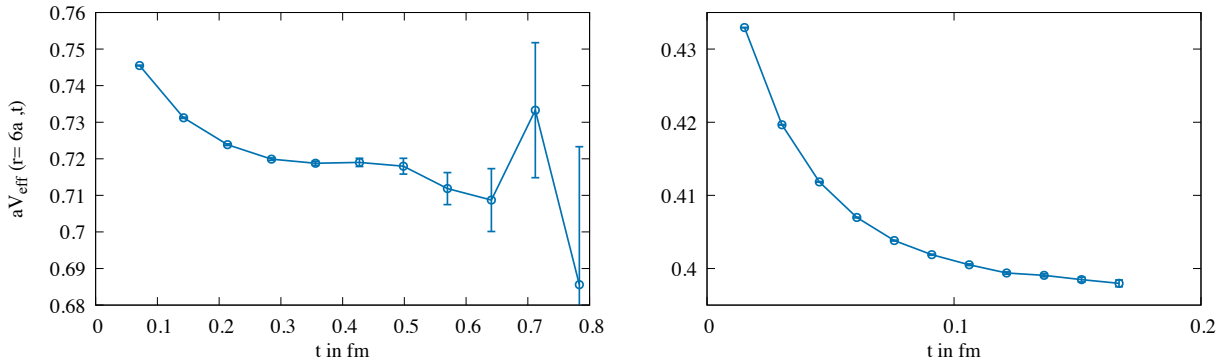

(a) $\beta = 2.50$. (b) $\beta = 3.00$.

Figure 4.2: $V_{\text{eff}}(r = 6a, t)$ at two different lattice spacings.

β	α	$a^2\sigma$	χ^2_{red}	a [fm]
2.50	0.2787(21)	0.03474(22)	0.8	0.0794(2)
2.70	0.2462(50)	0.00998(36)	0.6	0.0422(7)
2.85	0.2197(18)	0.00441(15)	0.4	0.0278(4)
3.00	0.1953(8)	0.00262(6)	1.0	0.0212(2)

Table 4.2: Parameters and reduced χ^2 of the fit with Cornell potential (2.12) to lattice data at different β. From these parameters the lattice constant a has been computed via Equation (2.35), identifying $r_0 = 0.5\,\text{fm}$.

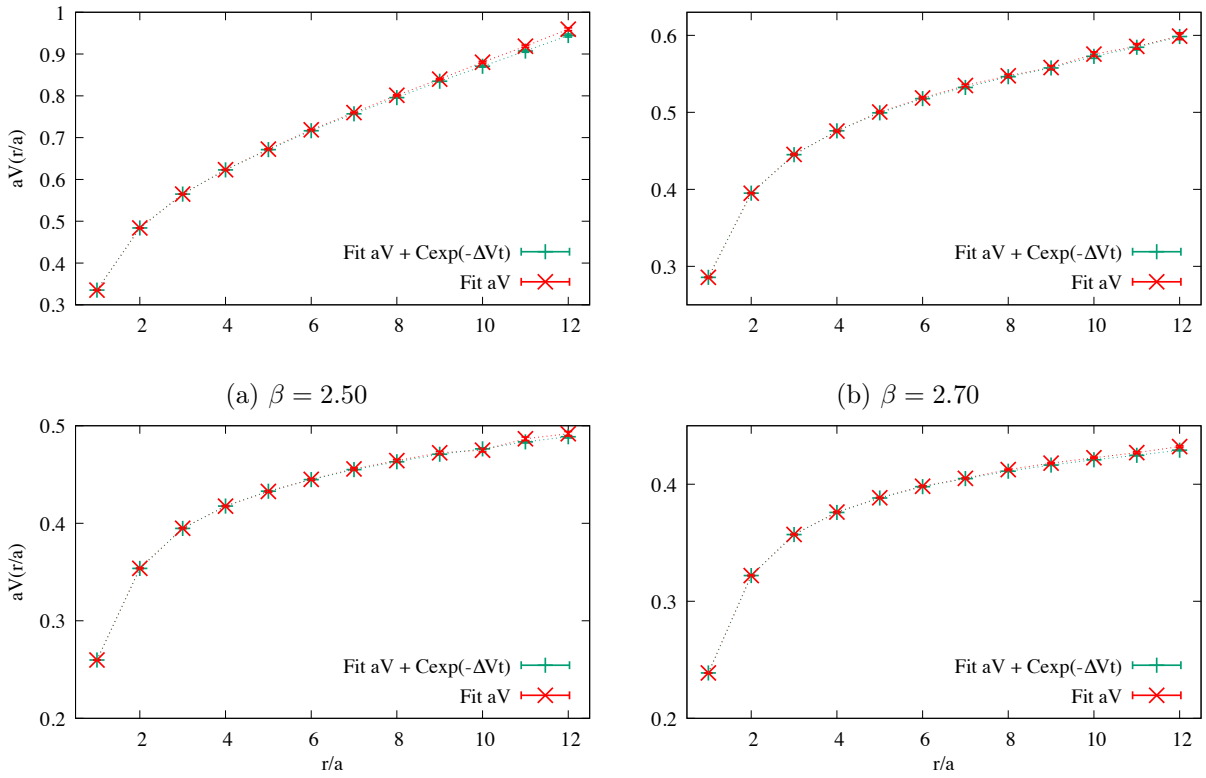

(a) $\beta = 2.50$ (b) $\beta = 2.70$

(c) $\beta = 2.85$ (d) $\beta = 3.00$

Figure 4.3: Ordinary static potential $aV(r/a)$ in lattice units at different β.

and $a(\beta = 2.70)$ are approximately equal to the estimates of [27]. The deviation to the gradient flow scale setting function increases with larger β. Neither the interpolating function from [26] nor the solutions of the renormalization group equation can describe all our data points. Hence, lattice spacings determined from either of the methods at large β should be treated with caution.

The lattice spacing needs to be set to enable the comparison of lattice results in physical units. Because the potential contains the self-energy of static quarks on the lattice, we shift the values by a relative constant so that the potential parametrizations coincide in their overlap region. Additionally, we shift all potentials such that $V_{\Sigma_g^+}(2r_0) = 0$. This shift is derived from the parametrization (2.12) of lattice data at $\beta = 2.50$.
The parametrizations are shown together with lattice data computed at different β in Figure 4.5. In Figure 4.5a, $a(\beta)$ is set according to the gradient flow scale setting function, whereas, in Figure 4.5b, the lattice spacings is set to the estimates in Table 4.2.
When lattice spacings are set to the larger estimates (Tab. 4.2), the long-distance behavior of all parametrizations approximately fit the lattice data at large r. This is not the case, when we set the lattice spacing to the smaller estimates (Tab. 2.3). Here, the slope of the short-distance parametrization deviates from the long-distance parametrization. This seems to support our lattice spacing estimates. However, it only relies on lattice data at very small separations.
As discussed earlier, one needs potential data at separations up to r_0 to gain reliable parameters for the scale setting via Equation (2.35). At large β, this requires the computation of large lattices.

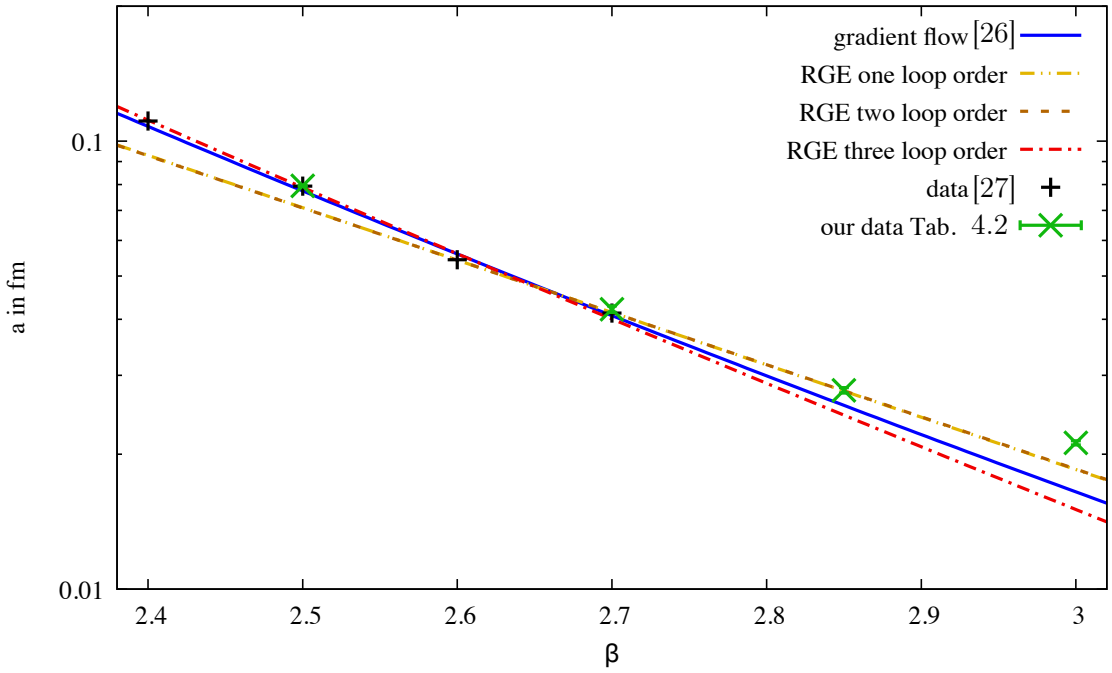

Figure 4.4: Different parametrizations of $a(\beta)$ with data points from the scale setting in [27] and our results from Table 4.2 on a logarithmic scale. Renormalization group equations (RGE) at one, two and three loop order are shown with dashed lines. The interpolating function from a scale setting via gradient flow is shown as a solid line.

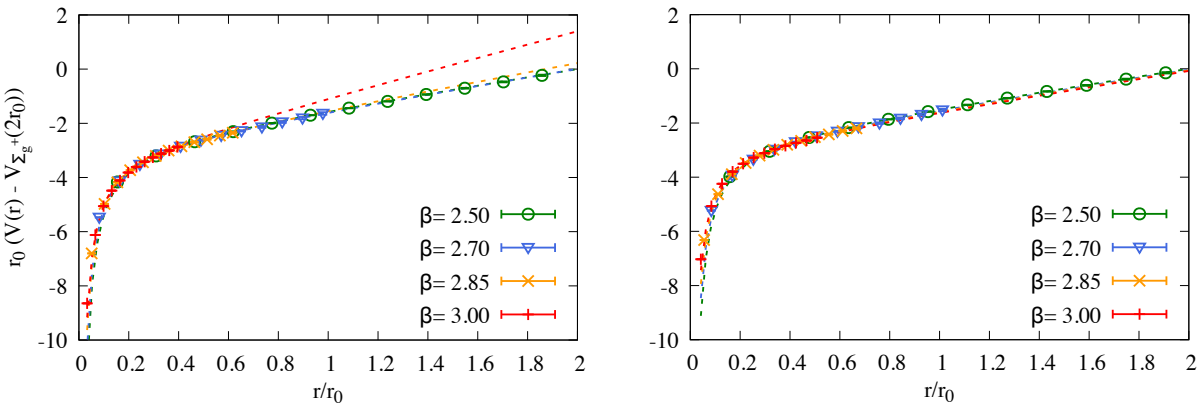

(a) Scale setting via gradient flow.

(b) Scale setting via Σ_g^+-parametrization.

Figure 4.5: Ordinary static potential Σ_g^+ computed at different β. Fits of Cornell potential to data points are shown as dashed lines.

4.2 Hybrid static potential Π_u

Next, we investigate the lowest hybrid static potential Π_u at small lattice spacings. As mentioned before, this observable is more complicated and shows larger statistical errors which complicates the extraction of the potential at small lattice spacings.

In Figure 4.6, the effective potentials are shown for each of the four lattice ensembles with $\beta = 2.50$, 2.70, 2.85 and 3.00.
Similar to the previous discussion, statistical errors increase with physical distance. Hence, the large time behavior of effective potentials at smaller β is hidden by large errors.
However, at $\beta = 2.50$ most excited states are suppressed already for smaller t/a, so that reasonable potential values can be extracted through a fit of the three-parameter function given in Equation (4.2) with fit parameters $aV(r)$, $C(r)$ and $\Delta V(r)$. At our smallest lattice coupling, results correspond to the plateaus, which are identified in a one-parameter fit with $aV(r)$ as the only fit parameter, within errors. Results from one- and three-parameter fits are compared in Figure 4.7.
In contrast to small β, the contribution of excited states is clearly visible in the effective potentials at larger lattice couplings. The effective potentials at $\beta = 2.85$ and 3.00 do not reach a plateau at the calculated temporal separations, especially at large spatial separations, r/a. This was already observed for the ordinary static potential.
In addition, the large time behavior of $V_{\text{eff}}(r/a, t/a)$ is hidden in noise which grows for complicated observables, as well.
On the one hand, fitting a constant definitly overestimates the potential. On the other hand, a fit with the three-parameter function (4.2) is reasonable only if the next higher state contributes to the effective potential. If many excited states are still dominant, the results of a three-parameter fit vary with the choice of fit range. Due to statistical errors, it is not possible to fit the effective potentials at large t/a, where excited states might be suppressed sufficiently. The only possibility to perform a reasonable fit is to consider the region of smaller statistical errors at small t/a.
The results lie below the one-parameter fit at small r/a, but might also underestimate the true potential value. At larger r/a, results approach the values from a one-parameter fit. Particularly, at $\beta = 2.85$ and $\beta = 3.00$, this effect can be seen in the data points at large r/a (Fig. 4.7c and 4.7d).
One could argue that the shape of the three-parameter fit results originates in a mixing with a decay of Π_u into the lowest glueball. But, owing to the reviewed difficulties in the application of the three-parameter fit (4.2) to the effective potential at small lattice spacings, this interpretation should be treated with caution.
Results from a one-parameter fit indicate the expected increase at small quark-antiquark distances [8], although values are probably shifted due to the contamination of excited states.

In Figure 4.8, data is shown in physical units. In the following, we compare results obtained from one- and three-parameter fits to the effective potential (shown in Fig. 4.8 at the top and bottom, respectively) and a scale setting via the gradient flow function and our lattice spacing results listed in Table 4.2 (left and right hand side of Fig. 4.8, respectively).
The relative shifts of the hybrid potentials are set similar to the ordinary static potential because the self-energy of static quarks is assumed to be the same on one lattice ensemble irrespective of

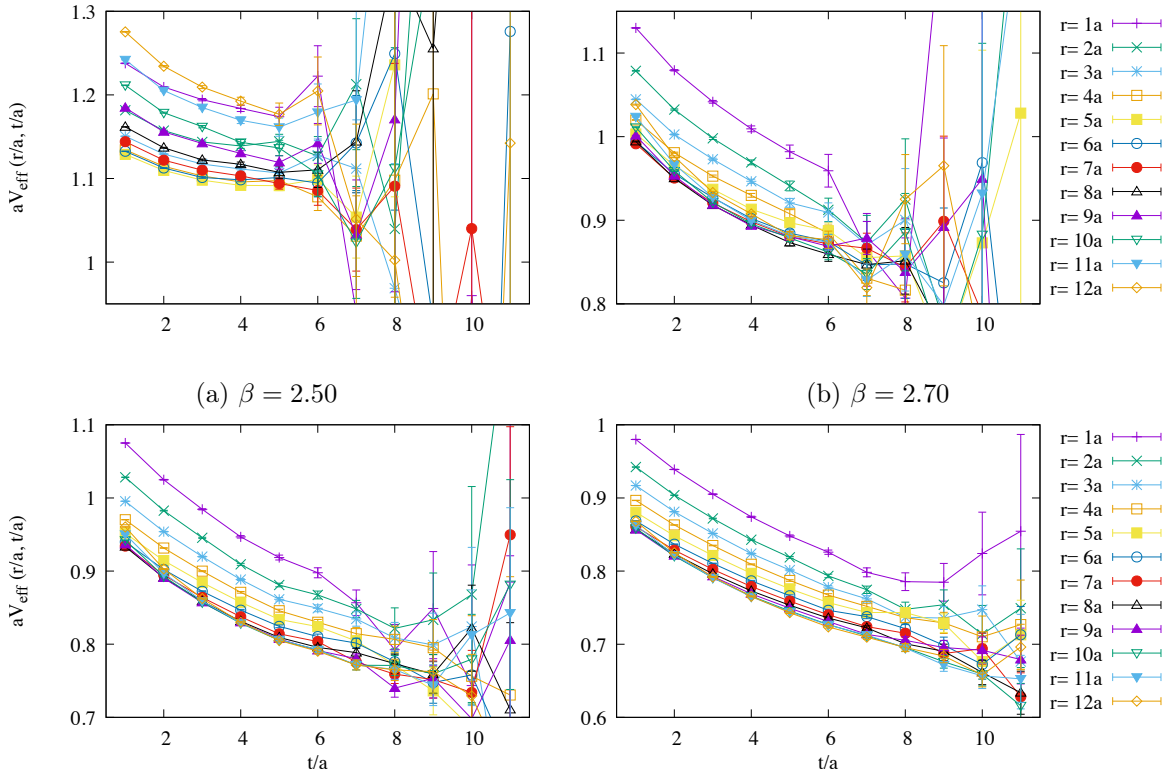

(a) $\beta = 2.50$ (b) $\beta = 2.70$

(c) $\beta = 2.85$ (d) $\beta = 3.00$

Figure 4.6: Effective potentials $aV_{\text{eff}}(r/a, t/a)$ for Π_u.

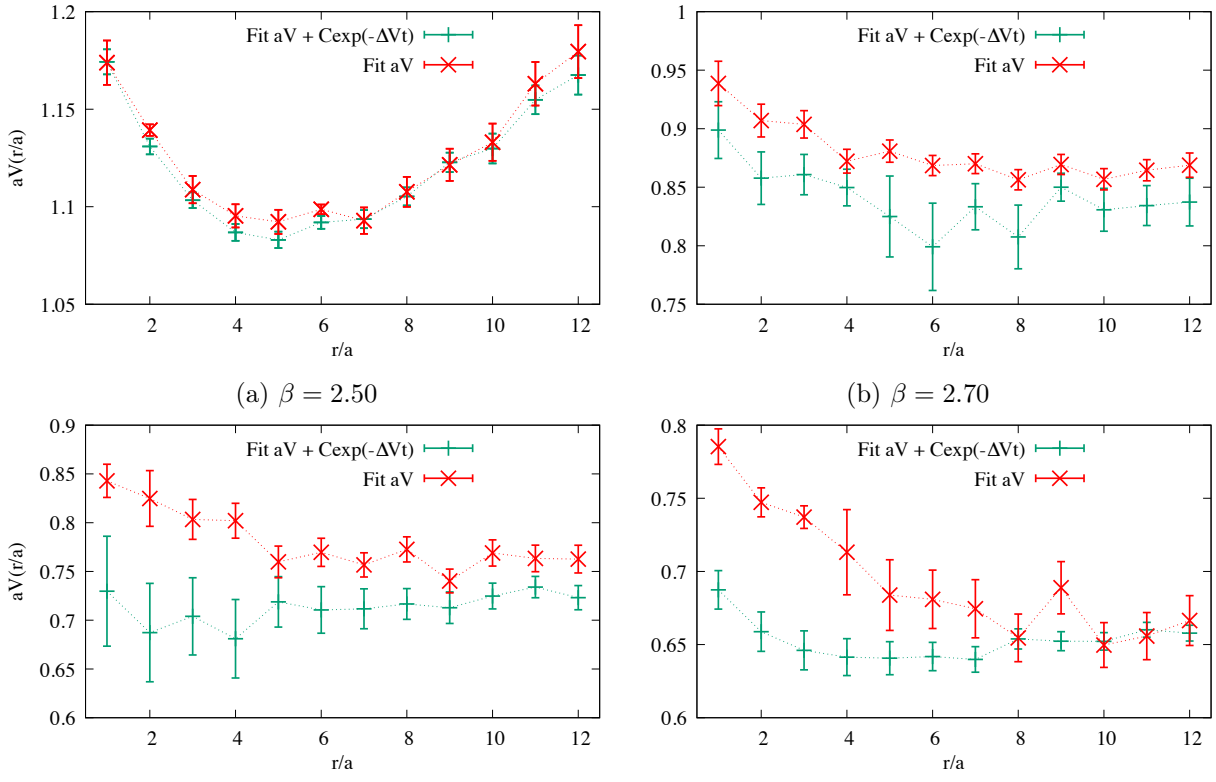

(a) $\beta = 2.50$ (b) $\beta = 2.70$

(c) $\beta = 2.85$ (d) $\beta = 3.00$

Figure 4.7: Ordinary static potentials $aV(r/a)$ in lattice units for each β.

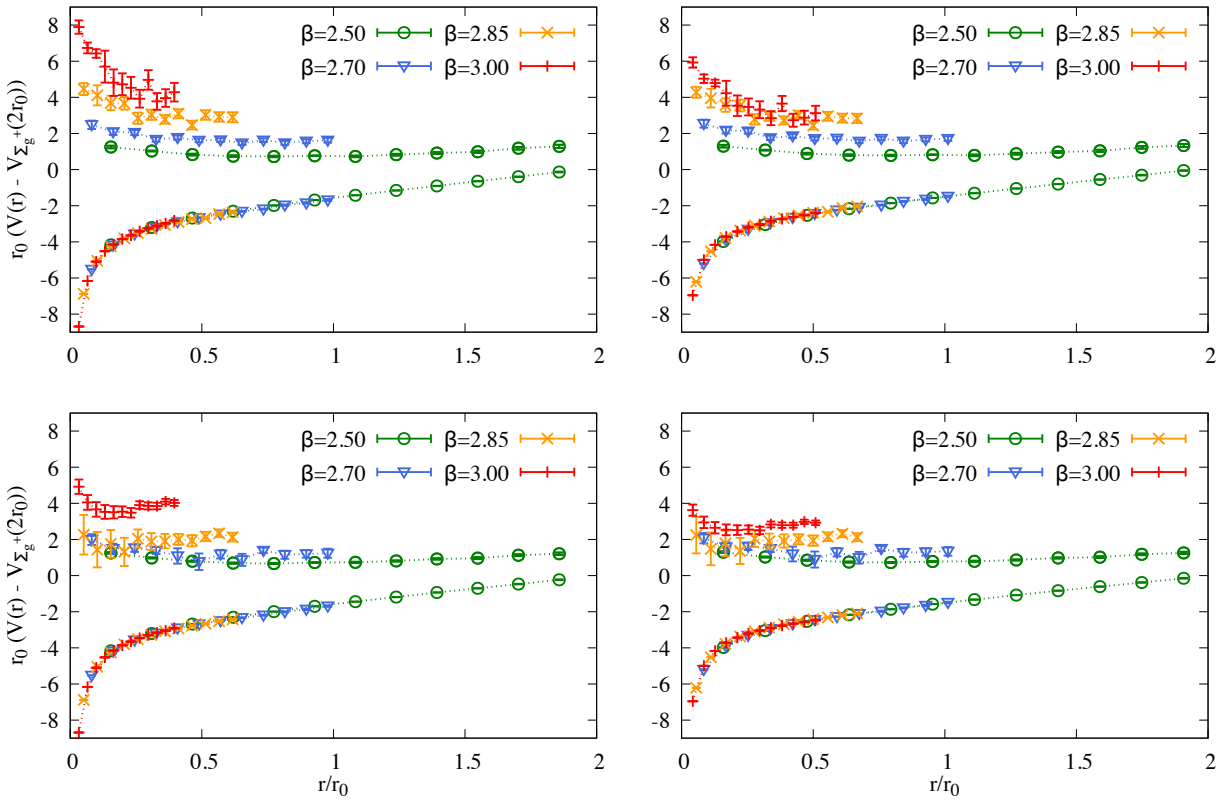

(a) Scale setting via gradient flow:
$a(2.50) = 0.0774\,\text{fm}$
$a(2.70) = 0.0408\,\text{fm}$
$a(2.85) = 0.0257\,\text{fm}$
$a(3.00) = 0.0165\,\text{fm}$

(b) Scale setting via ordinary static potential:
$a(2.50) = 0.0795\,\text{fm}$
$a(2.70) = 0.0422\,\text{fm}$
$a(2.85) = 0.0278\,\text{fm}$
$a(3.00) = 0.0212\,\text{fm}$

Figure 4.8: Lattice data of static potentials Σ_g^+ and Π_u at different lattice spacings in physical units.
Top: Results from one-parameter fit to effective potentials. Bottom: Results from three-parameter fit. Left: Scale setting via gradient flow. Right: Scale setting via ordinary static potential fit. Dotted lines between lattice data points are shown to guide the eye.

the observable.
We expect the hybrid static potentials at different lattice ensembles to coincide in their overlap regions. However, as discussed before, contamination by excited states causes a positive shift of lattice results. Since the situation becomes worse at smaller lattice spacings, the shift of data for short distances is greater. Results obtained from a one-parameter fit lie especially much higher than results from a three-parameter fit to the effective potential.
Comparing scale settings, it can be observed that the much smaller value of $a\,(\beta = 3.00)$ on the left hand side causes a greater displacement of the lattice data relative to the data obtained at smaller β. In the right plots, the relative shifts of lattice data of one lattice coupling to the next smaller one are comparable in size, which militates in favor of our determinations of lattice spacings. However, due to the difficulties in extracting the potential, one cannot rule out the smaller estimate. The lattice spacing might lie between both values. Therefore, the reliable determination of the lattice spacing at large β has to be one of the next steps in future investigations.

We assume the main source of error at small lattice spacing to be the fact that effective potentials do not reach their plateaus which already shows up for the ordinary static potential. Despite the positive shift in the hybrid static potential due to contributing excited states, the results indicate the expected repulsive behavior at small separations [8]. To get precise results for hybrid static potentials at small lattice spacings requires more measurements at larger temporal distances. Besides increasing the temporal distance, the groundstate overlap of hybrid operators could be improved further and better algorithms could be applied to improve potential results.

5 Glueballs at small lattice spacings

In the following, the mass computation of the lightest glueball 0^{++} at small lattice spacings is presented. This serves as a preparatory step for the analysis of correlation matrices to obtain lattice results for hybrid static potentials at short quark-antiquark distances, which are not contaminated due to a possible glueball decay.
Measurements are performed at three different lattice couplings, $\beta = 2.50$, 2.85 and 3.00. The lattice ensembles are the same as in the computation of static potentials, see Table 4.1.
Before the mass is extracted from a fit to the effective mass,

$$am_{\text{eff}}(t) = \ln\left(\frac{C(t)}{C(t+a)}\right), \tag{5.1}$$

the operator smoothing is optimized on all three lattices. The aim is to minimize the contribution from excited glueball states.

5.1 Optimization of blocking and smearing steps

Smearing and blocking, as explained in Section 2.4.2, can be combined in various ways to optimize the operator. The simplest combination is smearing of gauge links before performing a blocking procedure.
There are four parameters which can be chosen in the smoothing procedure. Two of them are the weight factors for the staples in the smearing and blocking equations, α_s and α_b, respectively. The other two parameters are the smoothing steps, N_s and N_b.
An increase of the weight factors can show a similar effect as an increase of the smearing or blocking steps. Hence, the weight factors are fixed to $\alpha_s = 0.5$ and $\alpha_b = 0.5$. The smearing steps N_s and the level of blocking N_b are left to be optimized aiming at an improved glueball operator overlap with the groundstate.

For each of the three lattice ensembles, the values N_s and N_b are varied to find the combination which minimizes the effective mass at $t = 0$. These computations were performed on a smaller subset of configurations than the final analysis of glueball mass. The results, $m_{\text{eff}}(t = 0)$, are presented in Figures 5.1a -5.1c. Each line corresponds to a fixed blocking level N_b. Fixing N_b, $m_{\text{eff}}(t = 0)$ is plotted against the level of smearing N_s.
It can be clearly seen that blocking of gauge links up to a certain level reduces the effective mass considerably. Whereas, smearing is able to adapt the operator size on a finer scale. This is the case at all lattice spacings.

For the lattice ensemble with $\beta = 2.50$ and lattice volume 48×24^3, the parameter N_b is varied from zero to four, N_s ranges from zero to eight. The lowest values are achieved with three times

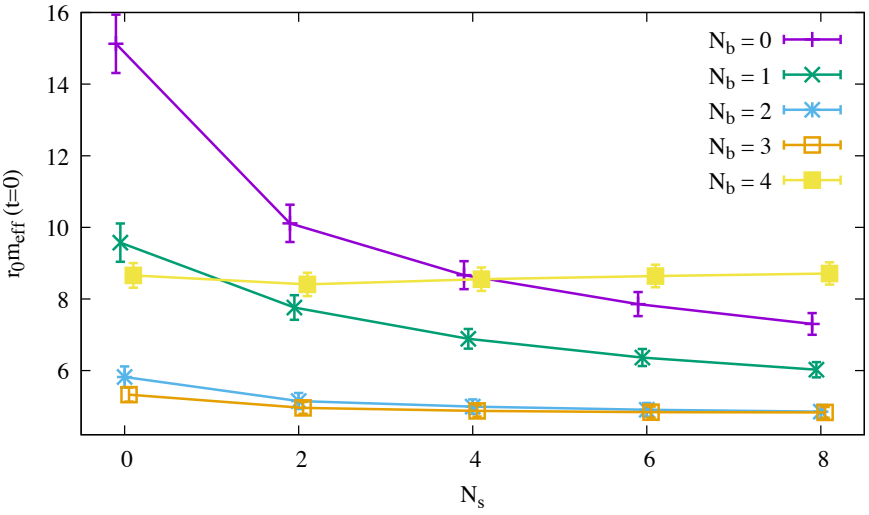

(a) $\beta = 2.50$, $T \times L^3 = 48a \times (24a)^3$.

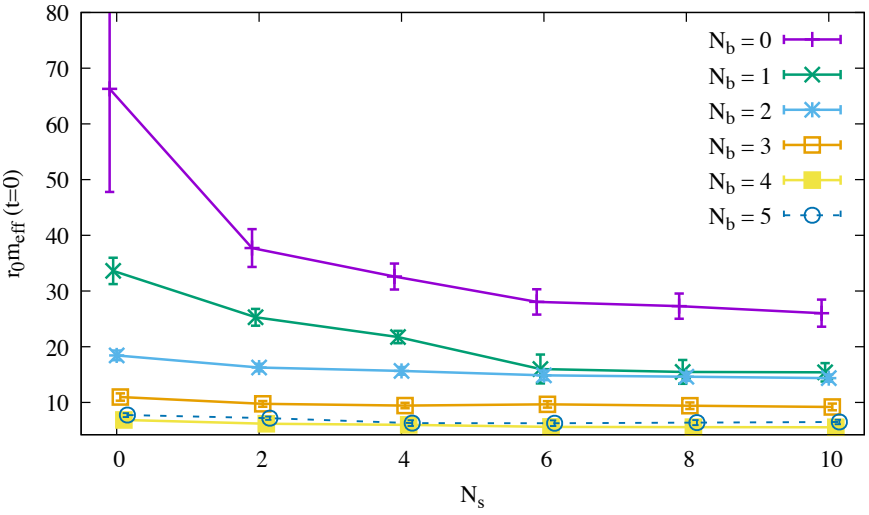

(b) $\beta = 2.85$, $T \times L^3 = 48a \times (26a)^3$.

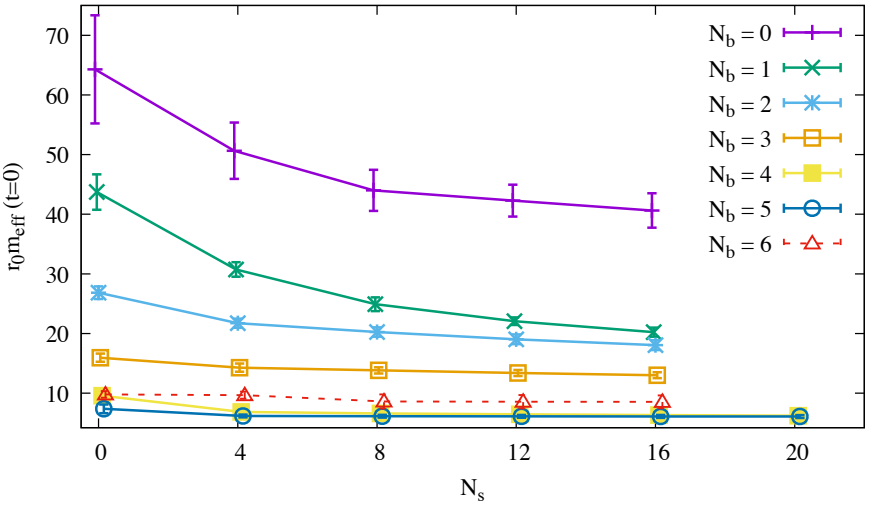

(c) $\beta = 3.00$, $T \times L^3 = 48a \times (34a)^3$.

Figure 5.1: Effective glueball mass $r_0 m_{\text{eff}}(t = 0)$ depending on the level of blocking N_b and smearing N_s.

blocking. In Figure 5.1a, $m_{\text{eff}}(t=0)$ calculated with $N_b = 4$ is shown, as well. Obviously, this worsens the groundstate overlap because the effective mass increases drastically.
We choose $N_s = 8$ to be the level of smearing used in the following computation of glueball mass, which results in the lowest effective mass in our analysis.
At $\beta = 2.85$, we add one more level of smearing, such that $N_s = 0, ..., 10$. $m_{\text{eff}}(t=0)$ with $N_b = 4$ lies lower than the results from less blocking steps. For $N_b = 4$, the smearing level $N_s = 4$ is chosen because higher smearing levels do not minimize the effective mass further within error.
In Figure 5.1c, at $\beta = 3.00$, it can be seen that blocking gauge links five times reduces the mass slightly in comparison to four times blocked gauge links. As before, the effective mass stays constant within error when more than 16 smearing steps are performed. Hence, we choose $N_s = 16$ for the following computations.

As discussed before, the blocking procedure elongates gauge links from which the glueball operator is computed. Their length after N_b blocking steps is $l_B = 2^{N_b}a$. If the length of one blocked link, l_B/a, exceeds the lattice extensions L/a, it winds around the lattice, hence, the same original gauge links contribute more than once due to periodic boundary conditions.
Four times blocking yields a gauge link length of $l_B = 2^4 a = 16a$. One more level would result in a length of $l_B = 2^5 a = 32a$. We note that the lattice extent at $\beta = 2.50$ and 2.85 is $L = 24a$ and $L = 26a$, respectively. Consequently, $N_b = 4$ is the highest possible blocking level for the two lattice ensembles without gauge link paths winding around the lattice. In the case of the finest lattice with $L/a = 34$ lattice sites, $N_b = 5$ is the largest blocking level. As can be seen in Figure 5.1b and 5.1c, where higher blocking steps are shown as dashed lines, further blocking increases the effective mass. This effect could either originate in the paths winding around the lattice or be caused by the size of the operator exceeding the physical size of the glueball's wave function. This is discussed in the following, based on a scale setting according to Table 4.2.

Smearing and blocking add contributions of neighboring gauge links to approach the physical size of the glueball's wave function. Whereas single-link smearing enlarges the size on a fine scale, blocking doubles the gauge link length in each step, increasing the operator volume faster. At $\beta = 2.50$, the chosen blocking level, $N_b = 3$, yields an operator with extension $l_B = 8a \approx 0.6\,\text{fm}$ in each spatial direction. The next higher level yields a spatial length of $l_B = 2^4 a \approx 1.3\,\text{fm}$, which drastically worsens the groundstate overlap. Furthermore, results with $l_B = 2^2 a \approx 0.3\,\text{fm}$ decrease to a similar low effective mass as with $N_b = 3$ if they are smeared sufficiently. Thus, one can infer that the optimal operator extension is $0.3\,\text{fm} < l \ll 1.3\,\text{fm}$.
At higher lattice coupling $\beta = 2.85$, the operator has a spatial extension of $l_B = 2^4 a \approx 0.4\,\text{fm}$ when choosing $N_b = 4$. The next level yields a length of $l_B = 2^5 a \approx 0.9\,\text{fm}$. This would narrow the optimal operator size to a length between 0.3 fm and 0.9 fm. However, it cannot be excluded that the increase in the effective mass is caused by the gauge link winding around the lattice. Therefore, $l_B = 2^5 a \approx 0.9\,\text{fm}$ sets a conditional upper boundary.
As expected, five blocking steps are necessary on the finer lattice, at $\beta = 3.00$. $N_b = 5$ at $\beta = 3.00$ means a gauge link length of $l_B = 32a \approx 0.7\,\text{fm}$. The slightly higher effective mass with an operator extent of $l_B = 2^4 \approx 0.3\,\text{fm}$ confirms the lower boundary.
In summary, we can determine the optimal glueball operator size to be $0.3\,\text{fm} < l \ll 1.3\,\text{fm}$. This specifies only a coarse range but it coincides with the typical glueball size (cf. e.g. [29]).

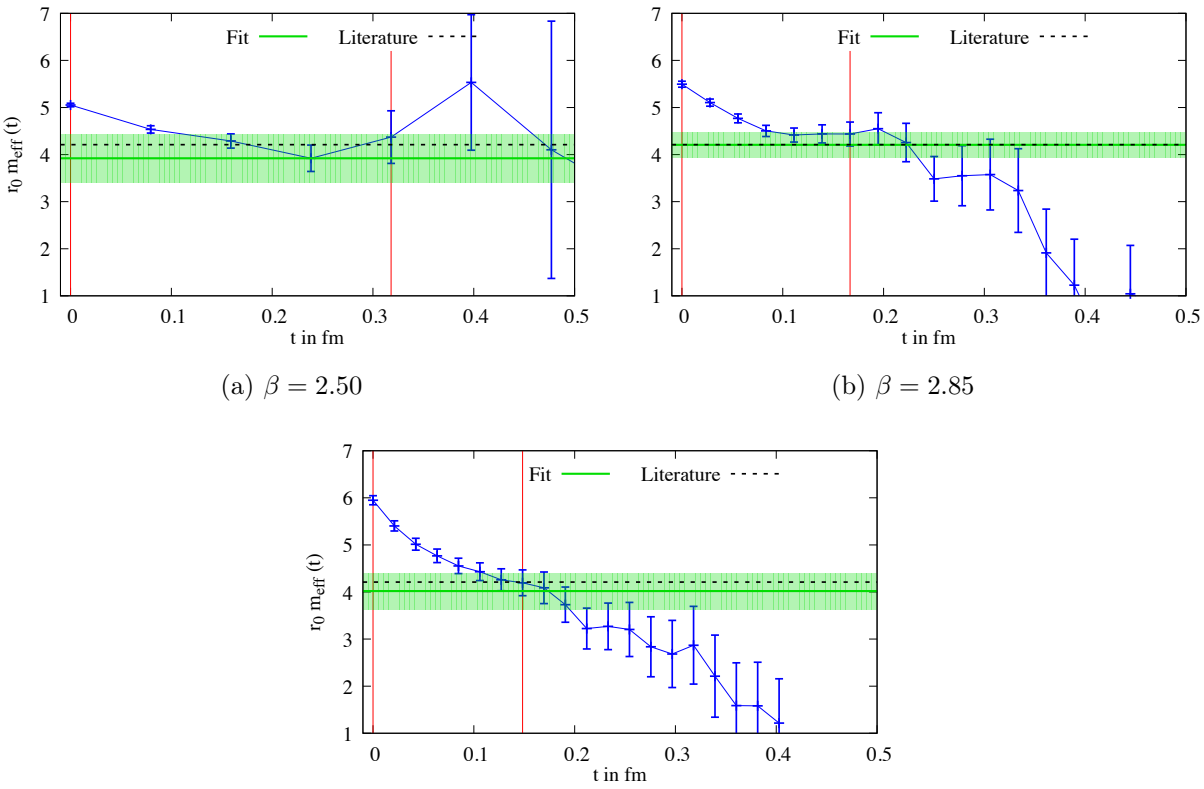

(a) $\beta = 2.50$

(b) $\beta = 2.85$

(c) $\beta = 3.00$

Figure 5.2: Effective glueball mass computed at different β (lines between lattice data to guide the eye). Literature value $r_0 m_{0^{++}} \approx 4.21$ [28] is shown as a dashed horizontal line. Result $r_0 m_{0^{++}}$ extracted via a three-parameter fit is presented with errorband in green. The fit range is delimited by vertical lines.

5.2 Glueball mass

The glueball operator given in Equation (2.30) is computed on three lattice ensembles with $\beta = 2.50$, 2.85 and 3.00, respectively, applying the optimal smoothing scheme determined in Section 5.1. We average the operator over the lattice volume yielding the rest mass of the lightest glueball, $m_{0^{++}}$.

Lattice results for the effective mass $r_0 m_{\text{eff}}(t)$ are presented in Figure 5.2.

As it is expected for the glueball observable, the statistical errors grow rapidly with time. Thus, a plateau in the effective mass at $\beta = 2.50$ is difficult to identify. Therefore, we perform a three-parameter fit, which includes a term for the contribution of excited states, similar to Equation (4.2). Fitting the three-parameter function to the first data points, where errors are still small, yields a reasonable mass at all β. Results are listed in Table 5.1 and illustrated in Figure 5.2 with an errorband. Glueball masses obtained in this work coincide within errors with the glueball mass from literature, $r_0 m_{0^{++}} \approx 4.21$ calculated in [28], when we identify the lattice spacings with our estimates from Table 4.2.

In conclusion, the single- and double-link smearing applied in the computation of glueball operator seem to suppress excited states sufficiently. Hence, the effective mass approaches the groundstate mass already at very small times.

In comparison to static potentials, the small lattice spacings in temporal direction ease the

β	2.50	2.85	3.00
(N_b, N_s)	$(3, 8)$	$(4, 4)$	$(5, 16)$
$am_{0^{++}}$	0.62(8)	0.23(2)	0.17(2)
$r_0 m_{0^{++}}$	3.9(5)	4.2(3)	4.0(4)

Table 5.1: Glueball masses extracted from a fit to the effective mass at different β. The optimized levels of blocking and smearing used in the computation of glueball operator are denoted by N_b and N_s, respectively. Scales are set according to Table 4.2.

computation of glueball mass as statistical errors are small. The physical size of the glueball's wave function can be adjusted on a coarse and fine scale by applying a combination of blocking and smearing of gauge links.

6 Conclusion

6.1 Summary

The aim of this work was the study of hybrid static potentials at small separations. The decay into a glueball and the ordinary static potential Σ_g^+ was discussed, which is energetically allowed at short quark-antiquark distances. In the course of this, the construction of glueball operators with angular momentum L_z and transformation properties similar to hybrid static potentials was shown in detail. This lead to the statement that hybrid static potentials $\Pi_u, \Pi_g, \Delta_g, \Sigma_u^+, \Delta_u$ and the first excitation of Σ_g^+ are allowed to decay into the lightest glueball. Σ_u^- and Σ_g^- are not affected by a decay into a 0^{++}-glueball due to the transformation properties of its creation operator.
For all channels, we examined the critical distance below which the minimum energy for the two decay products is reached and lattice results might be incorrect due to a decay (cf. Table 3.3).

The ordinary static potential Σ_g^+ and the lowest hybrid static potential Π_u were computed at four different lattice couplings, $\beta = 2.50$, 2.70, 2.85 and 3.00.
Besides the uncertainty in the determination of lattice scales at large β, the identification of plateaus in the effective potentials due to the small temporal extension at small lattice spacings, in particular for the hybrid potential, proved to be a main difficulty. Lattice results were compared for different fit methods and scale settings.
Additionally, we computed the mass of the lightest glueball 0^{++} at three different lattice couplings, $\beta = 2.50$, 2.85 and 3.00 with smoothed operators. For each lattice coupling, we found the optimal combination of subsequent smearing and blocking levels of gauge links used in the computation of the glueball operator. Moreover, the resulting glueball masses coincide within errors with the value from literature [28].

6.2 Outlook

This work provides the basis for an analysis of correlation matrices of hybrid potential operators and operators for a combined state of glueball and ordinary static potential. This will allow the reliable computation of hybrid static potentials at short quark-antiquark distances on the lattice without a contamination due to a possible glueball decay.
As a next step, an attempt should be made to improve the identification of plateaus in effective potentials at small lattice spacings. This could be achieved either by an improvement of the operator overlap to the groundstate, better algorithms or an increase of temporal separations. This can be attained e.g. through the simulation of anisotropic lattices with $a_t > a_s$.
Furthermore, the problem of scale setting at large β should be overcome e.g. by performing a scale setting via the gradient flow similar to [26].

Appendices

A Cylindrical wave expansion of plane waves

A.1 Solution of free Schrödinger equation in cylindrical coordinates

We consider a free particle. Its wavefunction can be found by solving the free time-independent Schrödinger equation

$$\frac{-1}{2m}\Delta\Psi(\vec{r}) = E\Psi(\vec{r}). \tag{A.1}$$

In cylindrical coordinates, the wavefunction depends on r, φ and z, $\Psi(\vec{r}) = \Psi(r, \varphi, z)$. The Schrödinger equation in cylindrical coordinates is

$$\frac{-1}{2m}\left[\frac{1}{r}\frac{\partial}{\partial r}\left(r\frac{\partial}{\partial r}\right) + \frac{1}{r^2}\frac{\partial^2}{\partial\varphi^2} + \frac{\partial^2}{\partial z^2}\right]\Psi(r,\varphi,z) = E\Psi(r,\varphi,z). \tag{A.2}$$

The wavefunction is separated in its variable dependence, the separation ansatz is

$$\Psi(r,\varphi,z) = R(r)\Phi(\varphi)Z(z). \tag{A.3}$$

Separation of variables yields

$$\frac{-1}{2m}\left[\frac{1}{rR(r)}\frac{\partial}{\partial r}\left(r\frac{\partial}{\partial r}R(r)\right) + \frac{1}{r^2\Phi(\varphi)}\frac{\partial^2}{\partial\varphi^2}\Phi(\varphi) + \frac{1}{Z(z)}\frac{\partial^2}{\partial z^2}Z(z)\right] = E. \tag{A.4}$$

The terms in brackets can be set equal to $-|\vec{k}|^2$.
Only the third term in brackets depends on the variable z, so it has to be constant independently. Reordering yields

$$\begin{aligned}\frac{1}{Z(z)}\frac{\partial^2}{\partial z^2}Z(z) &= -|\vec{k}|^2 - \frac{1}{rR(r)}\frac{\partial}{\partial r}\left(r\frac{\partial}{\partial r}R(r)\right) - \frac{1}{r^2}\frac{\partial^2}{\partial\varphi^2}\Phi(\varphi) &\text{(A.5)}\\ &= -k_z^2. &\text{(A.6)}\end{aligned}$$

The solution for $Z(z)$ is $Z(z) = e^{ik_z z}$.
Now, separating φ-dependent terms results in

$$\begin{aligned}\frac{1}{\Phi_l(\varphi)}\frac{\partial^2}{\partial\varphi^2}\Phi_l(\varphi) &= k^2r^2 - \frac{1}{R_l(r)}r\frac{\partial}{\partial r}\left(rR_l(r)\right) &\text{(A.7)}\\ &= -l^2, &\text{(A.8)}\end{aligned}$$

with $k^2 = |\vec{k}|^2 - k_z^2$. Again, both sides depend on different variables. The solution for $\Phi_l(\varphi)$ is $\Phi_l(\varphi) = e^{il\varphi}$ with $l \in \mathbb{Z}$. Finally, the differential equation for the radial wavefunction can be

written as

$$r\frac{\partial}{\partial r}\left(rR_l(r)\right) + \left[k^2r^2 - l^2\right]R_l(r) = 0. \tag{A.9}$$

Replacing $kr = \rho$ and interpreting R_l as a function of ρ, $R_l(\rho)$, yields

$$\frac{1}{\rho}\partial_\rho\left(\rho R_l(\rho)\right) + \left[1 - \frac{l^2}{\rho^2}\right]R_l(\rho) = 0 \tag{A.10}$$

which is the differential equation for Bessel functions. They are defined via

$$J_l(\rho) = \left(\frac{\rho}{2}\right)^l \sum_{j=0}^{\infty} \frac{(-1)^j}{j!\Gamma(l+j+1)}\left(\frac{\rho}{2}\right)^{2j}. \tag{A.11}$$

A solution of the free Schrödinger equation (A.1) in cylindrical coordinates is

$$\Psi(\vec{r}) = J_l(kr)e^{il\varphi}e^{ik_z z}. \tag{A.12}$$

with $k^2 + k_z^2 = |\vec{k}|^2$ being the squared momentum of the free particle which has energy $E = \frac{|\vec{k}|^2}{2m}$. If the transverse momentum k approaches zero, the Bessel function behaves like

$$J_l(kr \to 0) \approx \frac{1}{l!}\left(\frac{kr}{2}\right)^l \tag{A.13}$$

Consequently, for vanishing momentum, the wavefunction is non-zero only if the angular momentum along the z-axis, l, of the free particle is $l = 0$.

A.2 Expansion of plane waves

Plane waves, $e^{i\vec{k}\vec{r}}$, as a solution of the Schrödinger equation (A.1) can be expanded in terms of basis functions. In cylindrical coordinates, the plane wave can be written as

$$e^{i\vec{k}\vec{r}} = e^{ik_z z}e^{i\vec{k}_\perp\vec{r}_\perp}, \tag{A.14}$$

where "$\perp$" denotes the components perpendicular to the cylinder axis, $\vec{r}_\perp = (r, \varphi)$ and $\vec{k}_\perp = (k, \varphi_k)$. The z-independent part describes a plane wave travelling in the xy-plane. It can be expanded in terms of Bessel functions (A.11) [30]:

$$e^{i\vec{k}_\perp\vec{r}_\perp} = \sum_{l=-\infty}^{\infty} i^l J_l(kr)e^{il(\varphi-\varphi_k)}. \tag{A.15}$$

The complex conjugate is given by

$$e^{-i\vec{k}_\perp\vec{r}_\perp} = \sum_{l=-\infty}^{\infty} (-i)^l J_l(kr)e^{-il(\varphi-\varphi_k)}. \tag{A.16}$$

As a result, the plane wave can be written as

$$e^{-i\vec{k}\vec{r}} = e^{-ik_z z}\sum_{l=-\infty}^{\infty} (-i)^l J_l(kr)e^{-il(\varphi-\varphi_k)}. \tag{A.17}$$

A.3 Fourier transform of $J_l(kr)e^{il\varphi}$

With the definition

$$\Phi_{k,l}(r,\varphi) = J_l(kr)e^{il\varphi}, \tag{A.18}$$

Equation (A.17) is

$$e^{-i\vec{k}\vec{r}} = e^{-ik_z z} \sum_{l=-\infty}^{\infty} (-i)^l \Phi_{k,l}(r,\varphi)e^{il\varphi_k}. \tag{A.19}$$

From this, the Fourier transform of $\Phi_{k,l}$ can be found through the following steps [30].
Both sides of the above equation are first multiplied by $e^{-in\varphi_k}$ and then integrated over φ_k:

$$\frac{1}{2\pi}\int_0^{2\pi} \mathrm{d}\varphi_k\, e^{-in\varphi_k} e^{-i\vec{k}_\perp \vec{r}_\perp} = \frac{1}{2\pi}\int_0^{2\pi} \mathrm{d}\varphi_k \sum_{l=-\infty}^{\infty} (-i)^l \Phi_{k,l}(r,\varphi)e^{i(l-n)\varphi_k}. \tag{A.20}$$

With the orthogogonality relation

$$\frac{1}{2\pi}\int_0^{2\pi} \mathrm{d}\varphi\, e^{i(l-n)\varphi} = \delta_{ln}, \tag{A.21}$$

we can extract an equation for the function $\Phi_{k,n}(r,\varphi)$:

$$\Phi_{k,n}(r,\varphi) = \frac{1}{2\pi}\int_0^{2\pi} \mathrm{d}\varphi_k \left[i^n e^{-in\varphi_k}\right] e^{i\vec{k}_\perp \vec{r}_\perp}. \tag{A.22}$$

The insertion of $1 = \int \mathrm{d}k\, k\frac{\delta(k-k')}{k}$ yields

$$\Phi_{k,n}(r,\varphi) = \frac{1}{2\pi}\int_0^{2\pi} \mathrm{d}\varphi_k \int \mathrm{d}k\, k \left[i^n e^{-in\varphi_k}\frac{\delta(k-k')}{k}\right] e^{-i\vec{k}_\perp \vec{r}_\perp} \tag{A.23}$$

$$= \frac{1}{2\pi}\int \mathrm{d}^2k\ \tilde{\Phi}_{k,n}(k',\varphi_k)e^{-i\vec{k}_\perp \vec{r}_\perp}. \tag{A.24}$$

So

$$\tilde{\Phi}_{k,n}(k',\varphi_k) = i^n e^{-in\varphi_k}\frac{\delta(k-k')}{k} \tag{A.25}$$

is the two-dimensional Fourier transform of $\Phi_{k,l}(r,\varphi) = J_l(kr)e^{il\varphi}$. In summary, plane waves with the same wave number k but differently shifted phases can be superposed to give the cylindrical wave $\Phi_{k,l}$. Furthermore, the function $\sqrt{k}\,\Phi_{k,l}(r,\varphi)$ serves as the basis for the polar Fourier transform.

References

[1] S. L. Olsen, T. Skwarnicki and D. Zieminska, "Nonstandard heavy mesons and baryons: Experimental evidence," Rev. Mod. Phys. **90**, no. 1, 015003 (2018) [arXiv:1708.04012 [hep-ph]].

[2] E. Braaten, C. Langmack and D. H. Smith, "Selection Rules for Hadronic Transitions of XYZ Mesons," Phys. Rev. Lett. **112**, 222001 (2014) [arXiv:1401.7351 [hep-ph]].

[3] C. A. Meyer and E. S. Swanson, "Hybrid mesons," Prog. Part. Nucl. Phys. **82**, 21 (2015) [arXiv:1502.07276 [hep-ph]].

[4] E. S. Swanson, "XYZ states: theory overview," AIP Conf. Proc. **1735**, 020013 (2016) [arXiv:1512.04853 [hep-ph]].

[5] R. F. Lebed, R. E. Mitchell and E. S. Swanson, "Heavy-quark QCD exotica," Prog. Part. Nucl. Phys. **93**, 143 (2017) [arXiv:1610.04528 [hep-ph]].

[6] E. Braaten, C. Langmack and D. H. Smith, "Born-Oppenheimer Approximation for the XYZ Mesons," Phys. Rev. D **90**, no. 1, 014044 (2014) [arXiv:1402.0438 [hep-ph]].

[7] S. Capitani, O. Philipsen, C. Reisinger, C. Riehl and M. Wagner, "Precision computation of hybrid static potentials in SU(3) lattice gauge theory," Phys. Rev. D **99**, no. 3, 034502 (2019) [arXiv:1811.11046 [hep-lat]].

[8] M. Berwein, N. Brambilla, J. Tarrus Castella and A. Vairo, "Quarkonium hybrids with nonrelativistic effective field theories," Phys. Rev. D **92**, 114019 (2015) [arXiv:1510.04299 [hep-ph]].

[9] G. S. Bali and A. Pineda, "QCD phenomenology of static sources and gluonic excitations at short distances," Phys. Rev. D **69**, 094001 (2004) [hep-ph/0310130].

[10] K. J. Juge, J. Kuti and C. Morningstar, "Fine structure of the QCD string spectrum," Phys. Rev. Lett. **90**, 161601 (2003) [hep-lat/0207004].

[11] C. Gattringer and C. B. Lang, "Quantum chromodynamics on the lattice," Lect. Notes Phys. **788**, 1 (2010).

[12] H. J. Rothe, "Lattice gauge theories: An Introduction," [World Sci. Lect. Notes Phys. **82**, 1 (2012)].

[13] M. Albanese *et al.* [APE Collaboration], "Glueball Masses and String Tension in Lattice QCD," Phys. Lett. B **192**, 163 (1987).

[14] Cornwell, J.F., "Group Theory in Physics: An Introduction," Techniques of Physics, Elsevier Science (1997).

[15] M. Wagner, "Gruppentheoretische Methoden in der Physik: Ein Lehr- und Nachschlagewerk," Vieweg-Lehrbuch Mathematische Physik, Springer Berlin Heidelberg (2001)

[16] Albrecht Lindner, "Drehimpulse in der Quantenmechanik," Springer-Verlag (2013)

[17] Y. Chen *et al.*, "Glueball spectrum and matrix elements on anisotropic lattices," Phys. Rev. D **73**, 014516 (2006) [hep-lat/0510074].

[18] C. J. Morningstar and M. J. Peardon, "Efficient glueball simulations on anisotropic lattices," Phys. Rev. D **56**, 4043 (1997) [hep-lat/9704011].

[19] M. Teper, "An Improved Method for Lattice Glueball Calculations," Phys. Lett. B **183**, 345 (1987).

[20] B. Lucini, M. Teper and U. Wenger, "Glueballs and k-strings in SU(N) gauge theories: Calculations with improved operators," JHEP **0406**, 012 (2004) [hep-lat/0404008].

[21] M. Creutz, "Monte Carlo Study of Quantized SU(2) Gauge Theory," Phys. Rev. D **21**, 2308 (1980).

[22] R. Sommer, "A New way to set the energy scale in lattice gauge theories and its applications to the static force and alpha-s in SU(2) Yang-Mills theory," Nucl. Phys. B **411**, 839 (1994) [hep-lat/9310022].

[23] R. Sommer, "Scale setting in lattice QCD," PoS LATTICE **2013**, 015 (2014) [arXiv:1401.3270 [hep-lat]].

[24] S. Necco and R. Sommer, "The N(f) = 0 heavy quark potential from short to intermediate distances," Nucl. Phys. B **622**, 328 (2002) [hep-lat/0108008].

[25] M. Lüscher, "Properties and uses of the Wilson flow in lattice QCD," JHEP **1008**, 071 (2010) Erratum: [JHEP **1403**, 092 (2014)] [arXiv:1006.4518 [hep-lat]].

[26] T. Hirakida, E. Itou and H. Kouno, "Thermodynamics for pure SU(2) gauge theory using gradient flow," PTEP **2019**, no. 3, 033B01 (2019) [arXiv:1805.07106 [hep-lat]].

[27] O. Philipsen and M. Wagner, "On the definition and interpretation of a static quark antiquark potential in the colour-adjoint channel," Phys. Rev. D **89**, no. 1, 014509 (2014) [arXiv:1305.5957 [hep-lat]].

[28] C. J. Morningstar and M. J. Peardon, "The Glueball spectrum from an anisotropic lattice study," Phys. Rev. D **60**, 034509 (1999) [hep-lat/9901004].

[29] M. Loan, "Revisiting glueball wave functions at zero and finite temperature," Eur. Phys. J. C **54**, 475 (2008) [arXiv:0803.2894 [hep-lat]].

[30] Q. Wang, O. Ronneberger, and H. Burkhardt, "Fourier analysis in polar and spherical coordinates," Technical Report 1, IIF-LMB, Computer Science Department, University of Freiburg (2008)